Nonlinear Heat and Mass Transfer Resistivities for Liquid-Vapor Interfaces

by

Pouria Feyzi Oskouei

B.Sc., Sharif University of Technology, 2022

A Thesis Submitted in Partial Fulfillment of the Requirements for the Degree of

MASTER OF APPLIED SCIENCE

in the Department of Mechanical Engineering

University of Victoria

We acknowledge and respect the Lək̓ʷəŋən (Songhees and Xʷsepsəm/Esquimalt) Peoples on whose territory the university stands, and the Lək̓ʷəŋən and W̱SÁNEĆ Peoples whose historical relationships with the land continue to this day.

Nonlinear Heat and Mass Transfer Resistivities for Liquid-Vapor Interfaces

by

Pouria Feyzi Oskouei

B.Sc., Sharif University of Technology, 2022

Supervisory Committee

Dr. Henning Struchtrup, Supervisor

(Department of Mechanical Engineering)

Dr. Andrew Rowe, Committee Member

(Department of Mechanical Engineering)

Abstract

Nonlinear heat and mass transfer at liquid-vapor interfaces is studied, focusing on how interface resistivities vary with the intensity of non-equilibrium. Two distinct experimental approaches are considered: conventional experiments with relatively small mass and heat fluxes [G. Fang and C. A. Ward, Phys. Rev. E 59, 419 (1999)], and Molecular Dynamics (MD) experiments with relatively large fluxes [Homes, Simon and Vrabec, Jadran, Physics of Fluids 36, 2 (2024)]. This contrast leads us to the question: whether the strength of non-equilibrium impacts interface resistivities [Henning Struchtrup and Hans Christian Öttinger. Phys. Rev. E, 108(6):064801, 2023]. Based on a kinetic interface model, nonlinear resistivities are assessed in relation to interface temperature and the fluxes of mass and heat. The results show that for smaller fluxes, resistivities depend solely on local temperature, as is typically assumed in Linear Irreversible Thermodynamics. However, for larger fluxes, resistivities are influenced by the fluxes themselves as well.

Contents

List of Tables

List of Figures

Acknowledgments

Firstly, I would like to express my deepest appreciation to my supervisor, Dr. Henning Struchtrup, for his invaluable guidance, support, and encouragement throughout this research. His insights have been essential in shaping this work.

I am also grateful to my committee member, Dr. Andrew Rowe, for his valuable feedback and suggestions.

I would like to thank Dr. James McDonald from the University of Ottawa for serving as the external examiner. His thoughtful comment and suggestion led to a significant improvement in the quality of this thesis.

Additionally, I would like to thank Simon Homes and Jadran Vrabec for providing their detailed Molecular Dynamics data from Ref~[Homes, Simon and Vrabec, Jadran, Physics of Fluids 36, 2 (2024)], which contributed significantly to this study.

I am deeply indebted to my parents for their support not only throughout my academic journey but also all the stages in my life. Their belief in me has been a constant source of motivation.

Finally, I extend my gratitude to my friends and roommates who have offered their support and companionship along the way.

Chapter 1

Introduction

Evaporation and condensation are common both in everyday experiences and in various technological systems, such as vapor power plants and refrigeration systems. Despite their prevalence, the microscopic mechanisms and thermodynamic principles governing the processes at liquid-vapor interfaces particularly under nonequilibrium conditions, remain an area of ongoing investigation and limited understanding.

1.1 Experiments

Experimental observations have revealed notable temperature discontinuities and pressure deviations at the liquid-vapor interface during evaporation and condensation processes. Although these deviations are mostly visible in microscopic systems, remarkable temperature jumps were observed in macroscopic experiments [1, 3, 4, 5, 6, 7], challenging traditional hydrodynamic theories and earlier kinetic theory-based models which predicted smaller variations.

The setup Ward et al. used is shown in Fig. 1.1a; it involved a liquid droplet positioned in a funnel connected to a liquid reservoir, to measure the temperatures of both phases in the steady-state evaporation process [1]. In Fig. 1.1b, a significant temperature difference of 7.8K is observed at the liquid-vapor interface, where the vapor phase is at a higher temperature than the liquid. However, as noted, traditional hydrodynamic theory assumes no temperature discontinuity at the interface.

However, the assessment of physical experiments frequently struggles with substantial measurement inaccuracies. Specifically, errors in measuring pressure can equal or surpass the expected deviations from the saturation pressures observed in experimental results [8, 7].

Molecular dynamics (MD) simulations study heat and mass transfer at the liquid-vapor interface with molecular-level resolution. These simulations mimic the experimental setting with a stationary interface, where vapor particles are taken out and pumped back into the liquid. Unlike physical experiments, which are limited in capturing microscopic details, MD simulations provide direct access to resolved thermodynamic properties, such as density, temperature.

Figure 1.2 presents, from top to bottom, density and temperature profiles from a single evaporation scenario, simulation i.e., vanishing heat flux, taken from Ref. [2]. Within the Knudsen layer, which is locally non-equilibrium, the temperature separates into perpendicular $T_{\perp}$ and parallel $T_{\|}$ components. However, in local equilibrium the directional temperatures are all the same, equal to overall temperature. Similar to physical experiments, these simulations have shown large temperature difference between the bulk regions of liquid and vapor.

These disagreements with traditional hydrodynamic theory have sparked interest in refining thermodynamic models, particularly those focusing on interfacial resistivities and phase conversion coefficients [9].

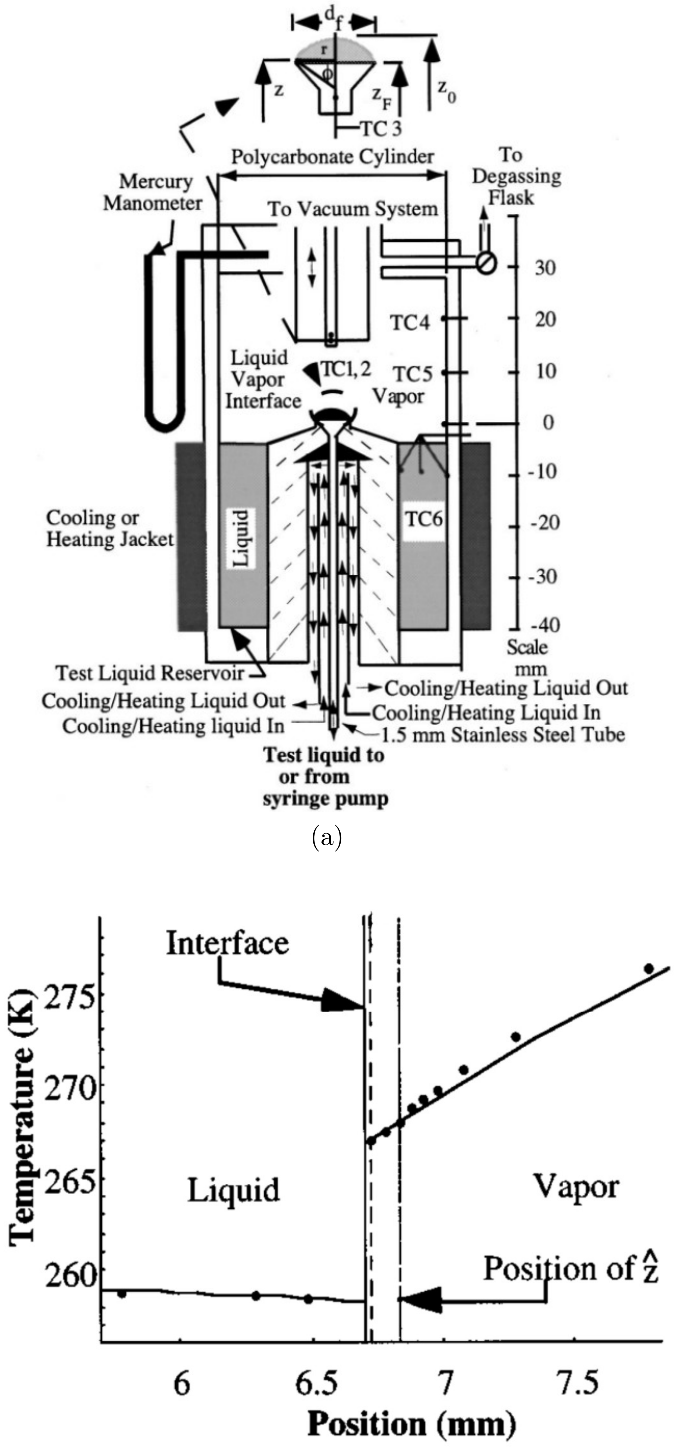

(a)

(b)

Figure 1.1: (a) Setup by Ward et al. taken from Ref. [1], for measuring phase temperatures at the droplet interface in steady state evaporation,
(b) A 7.8K temperature jump at the liquid-vapor interface, contradicting classical hydrodynamics.

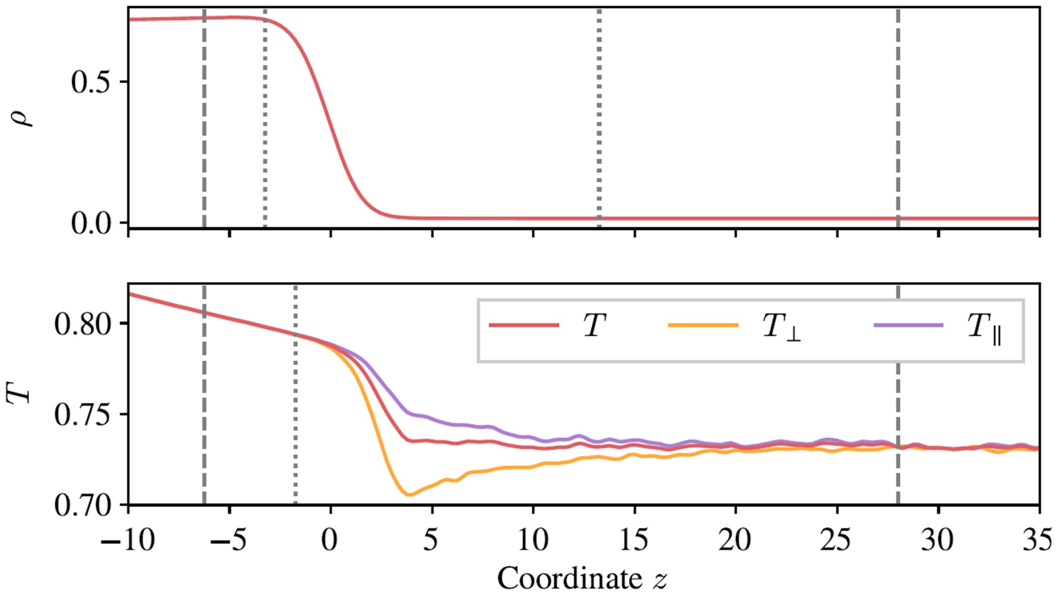

Figure 1.2: Spatial profiles taken from Ref. [2], for one simulation run of the evaporation scenario, i.e., vanishing heat flux. The graphs, from top to bottom, show density ρ and temperature T across the interface. In the Knudsen layer, the temperature splits into perpendicular $T_\perp$ and parallel $T_\parallel$ components. In local equilibrium the directional temperatures are all the same, equal to overall temperature T. The vertical lines show the boundaries of the interface region.

1.2 Thermodynamic Description and Kinetic Theory of Gases

The thermodynamic description of nonequilibrium interfaces is based on the principles of linear irreversible thermodynamics (LIT) [9]. This approach posits linear relationships between thermodynamic fluxes (both mass and energy) and their corresponding forces, i.e., the deviations in chemical potentials and temperatures between their adjacent bulk phases. Within the framework of LIT, interface resistivities, which only depend on interface temperature, are used to linearly connect these forces and fluxes [9]. Recently it was proposed that nonlinear force-flux relations might be required for processes in strong non-equilibrium [10]. The evaluation of this claim is the topic of this contribution.

The expressions for interface mass and heat fluxes (denoted as J and Q, respectively) are derived in Kinetic Theory of Gases through approximate solutions of the Boltzmann equation and suitable models for the liquid-vapor interface, e.g., via the Chapman-Enskog expansion or moment methods [11, 12]. These require an understanding of microscopic condensation probabilities which are classically assumed to be constant [13, 14, 15, 16, 17, 18]. However, in experimental simulations, Molecular Dynamics suggests that these probabilities vary with vapor particle impact energy and liquid surface temperature [19, 20, 21].

1.3 Purpose and Thesis Structure

Although Linear Irreversible Thermodynamics (LIT) assumes small deviations from equilibrium to maintain linearity between forces and fluxes, Molecular Dynamics (MD) simulations often exhibit significantly large evaporation fluxes [2]. This raises the possibility that such high fluxes could influence resistivities under conditions of intense non-equilibrium, contrasting with the linear regime where resistivities are solely functions of the local state [10].

In the following, the behavior of liquid-vapor interfaces is studied under the simplifying assumption that the vapor is an ideal gas using a general Kinetic Theory model that considers both constant and velocity-dependent condensation coefficients. Classical Kinetic Theory assumes that the condensation probability for vapor molecules hitting the liquid surface is constant. By including velocity-dependent coefficients inspired by Tsuruta's work [21], the model also includes cases where these coefficients depend on molecular motion and surface conditions. Based on this, macroscopic interface relations are derived and studied within the framework of Linear Irreversible Thermodynamics

(LIT). It is shown that under weak non-equilibrium conditions, resistivities are constant. However, for stronger non-equilibrium with higher fluxes, resistivities also depend on the fluxes themselves, as proposed in Ref. [10].

The remainder of this thesis is structured as follows:
Chapter 2 discusses the setup and the bulk equations, followed by a discussion of macroscopic and microscopic sharp interface models. Linear Irreversible Thermodynamics (LIT) provides a general framework [9], introducing interface resistivities as measurable parameters. The extended Hertz-Knudsen-Schrage (eHKS) model is explained [16, 17, 22, 23, 24], which is complemented by the heat transfer expression as well. Based on the eHKS the resistivities are determined and evaluated in order to study the nonlinearity with respect to the fluxes of mass and heat. Also, this chapter expands to a more complex model named Tsuruta, which uses velocity-dependent coefficients inspired by Tsuruta's work [21]. Based on the eHKS or Tsuruta model the resistivities are determined and evaluated in order to study the nonlinearity with respect to the fluxes of mass and heat.

Chapter 3 describes dimensionless formulation [25] used in this work and the value it offers in understanding the nonlinearity more clearly by eliminating the effect of local properties, i.e., interface temperature and the corresponding saturation pressure, on resistivities.

Chapter 4 examines resistivities using the eHKS Kinetic Theory model under Single-Flux case, i.e., vanishing mass flux or heat flux, with a wide range of fluxes consistent with recent studies flux ranges [2]. Then, the eHKS model is compared against a more refined Kinetic Thory model by Ytrehus and Cercignani [26, 27], here referred to as the Y/C model. In this model, the Knudsen layer is accounted for and it only considers the evaporation scenarios. This is to examine how much inaccuracy ignoring the Knudsen layer in the model can make. Additionally, it assumes a condensation coefficient of unity with no variation in other coefficients.

In Chapter 5, general cases are explored, with both fluxes occurring simultaneously, using an optimization method, to demonstrate the nonlinear interplay and influence of fluxes on resistivities. For general cases, due to the problem being undetermined, there are infinitely many possible solutions. With an appropriate initial guess and the governing equations provided through the objective function, the optimizer selects results that yield smooth and continuous functions for the resistivities. We introduce two approaches of Enforced-Symmetry and Unconstrained. In the former, Onsager symmetry in off-diagonal resistivities is satisfied under all conditions. However, in the latter, there is no assumption of off-diagonal symmetry enforced on the optimization. Therefore, in the Unguided results, Onsager symmtery is not expected.

In Chapter 6, the eHKS results are compared with a recent Molecular Dynamics (MD) study [2]. The results highlight that when going under large non-equilibrium conditions, resistivities not only vary with changes in the local state but are also influenced by the fluxes in the process.

In Chapter 7, resistivities are determined using the Tsuruta Model [21], where the condensation coefficient depends on particle impact velocity [18]. In the Tsuruta Model [21], an additional coefficient which accounts for the particle velocity, referred to as the Tsuruta coefficient ω, remarkably influences resistivities. The impact of this coefficient is explored within an acceptable range of this coefficient to understand its role in the resistivity matrix. First, Tsuruta coefficient's impact on the fluxes is discussed, next, this model is studied under the Single-Flux case.

Finally, Chapter 6 presents the conclusion along with recommendations for future research.

Regarding the appendices, in Appendix A, we demonstrate the simplification of the thermodynamic driving force for mass flux in the model, assuming an ideal gas and an incompressible liquid.

Appendix B further explains the extended Kinetic Model used in this study and the full flux and close-to-equilibrium resistivity expressions for the Tsuruta model are shown.

In Appendix C, the mass flux derivation in the Y/C interface model and the resistivity determination based on this model are discussed.

Lastly, Appendix D, the computed error is shown to verify the outputs (computed resistivities) of both optimization approaches of Enforced-Symmetry and Unguided.

Chapter 2

Macroscopic and Microscopic Interface Models

2.1 Linear Irreversible Thermodynamics

We focus on a one-dimensional, steady-state process with a planar interface separating the liquid and vapor bulk regions. Mass and heat transfer occur perpendicular to the interface with the system considered in a reference frame where the interface remains stationary as sketched in Fig. 2.1. To differentiate between the two phases subscripts l for liquid and v for vapor are used, respectively. Microscopically the interface layer has a diffusive structure with thickness of a few molecular diameters. Both in LIT and Kinetic Theory modelling the structure is not resolved, and the interface is considered as being a sharp change from liquid to vapor.

In one-dimensional steady state processes the overall mass flux J, momentum flux P and energy flux Q are constant. All flows are in the direction normal to the liquid-vapor interface. For evaporation or condensation processes, velocities are relatively small, hence higher orders of velocity in the balance of momentum and energy are ignored.

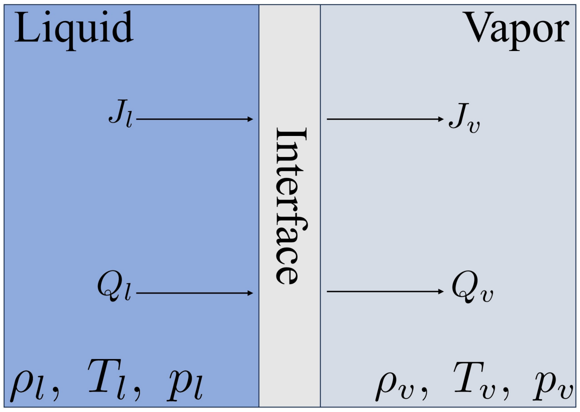

Figure 2.1: Schematic of liquid-vapor regions with the interface, experiencing nonequilibrium conditions by mass flux, J, and energy flux, Q, passing the interface. For the liquid region, the density ρ_l, and the temperature T_l and pressure p_l, for the vapor region, the density ρ_v, temperature T_v and the pressure p_l. Under steady-state conditions, the mass and energy fluxes in both phases equilibrate, $J = J_l = J_v$, $Q = Q_l = Q_v$

Additionally, we ignore viscous stresses in both heat flux and momentum flux. Thus, the conservation laws for mass ($\rho v = J =$ constant), momentum and energy read [9, 23]

$$J = J_l = J_v, \tag{2.1}$$

$$P = p_l = p_v, \tag{2.2}$$

$$Q = Jh_l + q_l = Jh_v + q_v. \tag{2.3}$$

Here, J, Q , h and q denote mass flux, energy flux, enthalpy and non-convective energy flux, respectively.

Evaporation and condensation processes are generally irreversible. Application of the second law of thermodynamics across the interface gives the interfacial entropy generation rate σ as

$$\sigma = J(s_v - s_l) + \frac{q_v}{T_v} - \frac{q_l}{T_l} \geq 0, \tag{2.4}$$

where s denotes entropy and $\frac{q}{T}$ is the bulk conductive entropy flux [9, 25]. The entropy generation σ vanishes in liquid-vapor equilibrium states and assumes positive values in non-equilibrium.

By eliminating the conductive heat flux in the liquid q_l using (2.3) in (2.4) the entropy generation rate becomes

$$\sigma = J\left[\frac{g_l}{T_l} - \frac{g_v}{T_v} + h_v\left(\frac{1}{T_v} - \frac{1}{T_l}\right)\right] + q_v\left[\frac{1}{T_v} - \frac{1}{T_l}\right] \geq 0, \tag{2.5}$$

where $g = h - Ts$ denotes Gibbs free energy. We follow the principles of LIT [9], in which the entropy generation rate is interpreted as a sum of products of thermodynamic fluxes and forces

$$\sigma = \sum_{\alpha} J_\alpha F_\alpha \geq 0, \tag{2.6}$$

where we identify the fluxes

$$J_\alpha = \{J, q_v\}, \tag{2.7}$$

and the forces

$$F_\alpha = \{F_J,\ F_Q\} = \left\{\frac{g_l}{T_l} - \frac{g_v}{T_v} + h_v\left(\frac{1}{T_v} - \frac{1}{T_l}\right),\ \frac{1}{T_v} - \frac{1}{T_l}\right\}. \tag{2.8}$$

The entropy generation rate must be non-negative for all processes, and vanish in equilibrium. In LIT this is guaranteed by a linear phenomenological ansatz

$$F_\alpha = \sum_{\beta} r_{\alpha\beta} J_\beta, \tag{2.9}$$

with the non-negative definite matrix of resistivities $r_{\alpha\beta}$, which is expected to be symmetric due to Onsager's principle [9, 18, 28, 29, 30, 31].

Typically, in LIT it is assumed that the resistivity matrix depends on the local temperature only, for which one either chooses the temperature of the liquid at the interface

(T_l), or a separate interface temperature (T_s). The detailed discussion in [10] showed that both temperatures are expected to be rather close, and in the following we consider the liquid temperature T_l as the relevant temperature for the description of the interface. Moreover, in [10] it was argued that for cases of strong equilibrium the resistivities will depend not only on the local equilibrium state through the chosen temperature, but also on the local nonequilibrium state through the fluxes passing through the interface.

To proceed, we use the liquid temperature to rewrite the force-flux relation (2.9) with a dimensionless matrix of resistivities $\hat{r}_{\alpha\beta}$, defined as [18, 32]

$$\begin{aligned} \hat{r}_{11} &= \tfrac{p_{\text{sat}}(T_l)}{R\sqrt{2\pi RT_l}} r_{11} \quad , \qquad \hat{r}_{12} = \tfrac{p_{\text{sat}}(T_l)T_l}{\sqrt{2\pi RT_l}} r_{12} \\ \hat{r}_{21} &= \tfrac{p_{\text{sat}}(T_l)T_l}{\sqrt{2\pi RT_l}} r_{21} \quad , \qquad \hat{r}_{22} = \tfrac{p_{\text{sat}}(T_l)RT_l^2}{\sqrt{2\pi RT_l}} r_{22}, \end{aligned} \tag{2.10}$$

where $p_{\text{sat}}(T_l)$ denotes the equilibrium saturation pressure of the evaporating fluid at T_l, and R is its gas constant. The factor $\sqrt{2\pi}$ is inspired by the Kinetic Theory of gases expressions [25], which are shown in the next section. With this, the force-flux relations assume the form

$$\begin{bmatrix} F_J \\ F_Q \end{bmatrix} = \begin{bmatrix} \frac{g_l}{RT_l} - \frac{g_v}{RT_v} + h_v \left(\frac{1}{RT_v} - \frac{1}{RT_l} \right) \\ \frac{T_l}{T_v} - 1 \end{bmatrix} = \begin{bmatrix} \hat{r}_{11} & \hat{r}_{12} \\ \hat{r}_{21} & \hat{r}_{22} \end{bmatrix} \begin{bmatrix} \frac{\sqrt{2\pi RT_l}}{p_{\text{sat}}(T_l)} J \\ \frac{\sqrt{2\pi RT_l}}{p_{\text{sat}}(T_l)} \frac{q_v}{RT_l} \end{bmatrix}, \tag{2.11}$$

where all revised forces and fluxes are dimenssionless.

The above relation (2.11) reduces significantly for the case of small deviations from equilibrium, for which Taylor expansion and use of thermodynamic property relations lead to

$$\begin{bmatrix} \frac{\Delta p}{p_{\text{sat}}(T_l)} \\ -\frac{\Delta T}{T_l} \end{bmatrix} = \begin{bmatrix} \hat{r}_{11} & \hat{r}_{12} \\ \hat{r}_{21} & \hat{r}_{22} \end{bmatrix} \begin{bmatrix} \frac{\sqrt{2\pi RT_l}}{p_{\text{sat}}(T_l)} J \\ \frac{\sqrt{2\pi RT_l}}{p_{\text{sat}}(T_l)} \frac{q_v}{RT_l} \end{bmatrix}. \tag{2.12}$$

Here, $\Delta p = p - p_{\text{sat}}(T_l)$ denotes deviation of actual pressure in the vapor p from saturation, and $\Delta T = T_v - T_l$ is the temperature jump across the interface.

Under the assumptions of a monatomic ideal gas for the vapor phase, an incompressible liquid, and a negligible specific volume of the liquid v_l compared to the vapor v_v, the force-flux relation reduces to

$$\begin{bmatrix} F_J \\ F_Q \end{bmatrix} = \begin{bmatrix} \frac{5}{2}\left(1 - \frac{T_V}{T_L} + \ln\left(\frac{T_V}{T_L}\right)\right) - \ln\left(\frac{p}{p_{\mathrm{sat}}(T_l)}\right) \\ \frac{T_l}{T_v} - 1 \end{bmatrix} = \begin{bmatrix} \hat{r}_{11} & \hat{r}_{12} \\ \hat{r}_{21} & \hat{r}_{22} \end{bmatrix} \begin{bmatrix} \frac{\sqrt{2\pi R T_l}}{p_{\mathrm{sat}}(T_l)} J \\ \frac{\sqrt{2\pi R T_l}}{p_{\mathrm{sat}}(T_l)} \frac{q_v}{R T_l} \end{bmatrix}; \tag{2.13}$$

see Appendix A for details on derivation of the force F_J.

LIT does not provide further insight for determining the values of $\hat{r}_{\alpha\beta}$. Therefore, these coefficients are determined utilizing either experimental measurements or theoretical models.

With four resistivities (or three, assuming Onsager symmetry [28]) in the two governing equations (2.13), it is not possible to determine all resistivities from a single experiment or simulation. To address this, simplified process settings where either $J = 0$ or $q_v = 0$ are often used, allowing for the determination of two resistivities in a single experiment. These configurations are commonly applied in molecular dynamics (MD) simulations [2, 33].

2.2 Interface Models for Kinetic Theory

The evaluation of physical experiments often encounters significant measurement errors. Notably, the error associated with pressure measurement can be as large, if not larger, than the anticipated experimental deviation from saturation pressures [8, 7]. Moreover, these experiments are generally limited to relatively low fluxes. Consequently, theoretical approaches serve as alternatives for determining resistivities.

In the intuitive Maxwell interface model one considers simplified processes for particles as follows [23]:

The condensation coefficient is defined as the probability that a vapor particle will condense upon reaching the interface. This is depicted in Fig. 2.2 by the vertical arrow pointing towards the interface. Conversely, the probability that a particle reflects rather than condenses is $1 - \psi$, accounting for the reflected molecules shown in Fig. 2.2. We follow the classical Maxwell model [23] in which rebounding molecules are either specularly or diffusively reflected. In a specular reflection, the normal momentum is inverted while tangential momentum and energy are conserved, while in a diffusive reflection, the particle engages in thermal exchanges with the other particles in the interface. The accommodation coefficient γ is defined as the relative amount of diffuse reflections, i.e., $\gamma = 0$ and $\gamma = 1$ indicate pure specular and pure diffuse reflection, respectively.

One of the most celebrated interface models is classical Hertz-Knudsen-Schrage (HKS) model [16, 17, 22], that is a Kinetic Theory model with a constant condensation coefficient. Based on the classical HKS model, the mass flux reads

$$J_{HKS} = \frac{2\psi}{2-\psi}\left[\frac{p_{\mathrm{sat}}(T_l)}{\sqrt{2\pi R T_l}} - \frac{p}{\sqrt{2\pi R T_v}}\right]. \tag{2.14}$$

Typically, the classical HKS is shown only by its mass flux. However, for the full computation of the evaporation and condensation processes, one needs interface condition for both fluxes of mass and energy. Therefore, the classical HKS needs a corresponding expression for the heat flux.

The suggested corresponding heat flux based on a simplified kinetic model [18, 23] reads

$$\frac{q_{v,\mathrm{HKS}}}{RT_l} = \frac{2\psi}{2-\psi}\left(2 - \frac{5}{2}\frac{T_v}{T_l}\right)\left[\frac{p_{sat}(T_l)}{\sqrt{2\pi R T_l}} - \frac{p}{\sqrt{2\pi R T_v}}\right] + \frac{4\psi(1-\gamma)+\gamma}{2-\psi(1-\gamma)-\gamma} p \left[1 - \frac{T_v}{T_l}\right]\sqrt{\frac{1}{2\pi R T_v}}. \tag{2.15}$$

We account for the nonlinear mass flux with higher order terms in the Maxwellian

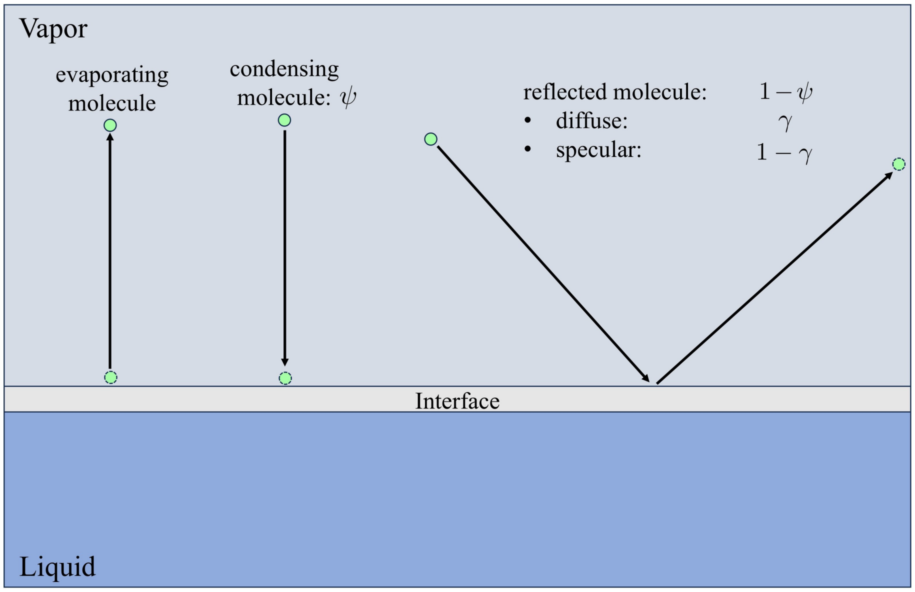

Figure 2.2: Different types of particle interaction with the interface.

approximation, which is the extension of the Ref [18], see Appendix B for details.

Based on this model, the extended HKS (eHKS) mass flux reads [23]

$$J_{eHKS} = \frac{2\psi}{2-\psi}\left[\frac{p_{\text{sat}}(T_l)}{\sqrt{2\pi RT_l}} - \frac{p}{\sqrt{2\pi RT_v}} - \frac{1}{2\sqrt{2\pi}}\frac{\sqrt{RT_v}}{p}J^2\right], \tag{2.16}$$

which is similar to the classical HKS mass flux in (2.14), but with an extra quadratic term $-\frac{1}{2\sqrt{2\pi}}\frac{\sqrt{RT_v}}{p}J^2$ to account for the nonlinear effect in the mass flux.

Subsequently, the eHKS heat flux flux reads

$$\begin{aligned}\frac{q_{v,eHKS}}{RT_l} &= \frac{2\psi}{2-\psi}\left(2-\frac{5}{2}\frac{T_v}{T_l}\right)\left[\frac{p_{\mathrm{sat}}(T_l)}{\sqrt{2\pi RT_l}}-\frac{p}{\sqrt{2\pi RT_v}}\right]+\frac{4\psi(1-\gamma)+\gamma}{2-\psi(1-\gamma)-\gamma}\left[1-\frac{T_v}{T_l}\right]\frac{p}{\sqrt{2\pi RT_v}} \\ &+ 8\pi^2\frac{\psi(1-\gamma)+\gamma}{2-\psi(1-\gamma)-\gamma}\left[\frac{1-\psi}{2-\psi}\frac{8\gamma}{\gamma+(1-\gamma)\psi}\left(\frac{p}{\sqrt{2\pi RT_v}}\left(1-\frac{7T_v}{4T_l}\right)\right.\right. \\ &\left.\left. + \frac{1}{2}\frac{p_{\mathrm{sat}}(T_l)}{\sqrt{2\pi RT_l}}\frac{T_v}{T_l}\right)-\frac{1}{\sqrt{2\pi RT_l}}\left(p+2p_{\mathrm{sat}}(T_l)\sqrt{\frac{T_v}{T_l}}\right)\right]\frac{2\pi\sqrt{RT_v}^{3/2}}{p^2}\frac{1}{\sqrt{RT_l}}J^2 \\ &+ \frac{1}{\sqrt{8\pi}}\frac{\psi}{2-\psi}\frac{(RT_v)^{5/2}}{p^3}\frac{1}{2RT_l}J^4,\end{aligned}\tag{2.17}$$

which is similar to the classical HKS heat flux in (2.15), but with two extra nonlinear mass flux terms:

1- Quadratic term associated with the second and third lines of Eq. (2.17),

2- Quartic term in the last line of Eq. (2.17).

Specifically, in the derivation of this model Knudsen layers were ignored, which introduces some deviation in comparison to accurate Kinetic Theory computations [27, 34]. The model is useful for our purpose, since it provides explicit nonlinear force-flux relations for further evaluation.We note that while evaporation and accommodation coefficients are intuitive in principle, they describe microscopic interactions and thus cannot be directly measured in experiments. Instead, macroscopic experiments as well as MD simulations determine macroscopic properties such as temperatures, densities, pressures and heat and mass fluxes, which can only be linked to the microscopic interface coefficients through models such as the above.

Popular Kinetic Theory models rely on condensation and accommodation coefficients as constants [14]. For example, in the classical Hertz and Knudsen theories, the condensation coefficient is assumed to be unity [16, 17], and more recent studies similarly conclude that an evaporation coefficient of unity suffices [33].

These flux equations are inherently nonlinear functions of the bulk liquid and vapor properties adjacent to the interface, resulting in nonlinearity between forces and fluxes. Also, these equations are in a different form that is shown by LIT in (2.13) meaning that the eHKS model does not match with the LIT force-flux relations in (2.11), nevertheless, it implicitly will allow determination of nonlinear resistivities.

Moreover, since we consider higher-order mass flux terms in the eHKS fluxes Eq. (2.16) and (2.17), one can include the higher term of velocity (or mass flux) in the balance of energy Eq. (2.3) to re-define the thermodynamic forces, particularly $\hat{F}_J$ in Eq. (2.8). However, this only results in a change in the definition of resistivities, therefore, including higher terms of velocity in $\hat{F}_J$ is only a matter of choice.

In the linear limit under Linear Irreversible Thermodynamics (LIT), a first-order Taylor expansion yields the corresponding resistivities in the linear limit as [18, 10, 23]

$$\hat{r}_{\alpha\beta}^{eHKS} = \begin{bmatrix} \frac{1}{\psi} - \frac{7}{16}\left(\frac{1-\frac{9}{7}(1-\gamma)(1-\psi)}{\gamma+\psi(1-\gamma)}\right) & \frac{1}{8}\left(\frac{2-\gamma-\psi(1-\gamma)}{\gamma+\psi(1-\gamma)}\right) \\ \frac{1}{8}\left(\frac{2-\gamma-\psi(1-\gamma)}{\gamma+\psi(1-\gamma)}\right) & \frac{1}{4}\left(\frac{2-\gamma-\psi(1-\gamma)}{\gamma+\psi(1-\gamma)}\right) \end{bmatrix}. \tag{2.18}$$

As previously noted, these resistivity matrices conform to the Onsager symmetry principle [28].

For the case of fully diffusive reflection $\gamma = 1$, the resistivities reduce to

$$\hat{r}_{\alpha\beta}^{eHKS} = \begin{bmatrix} \frac{1}{\psi} - \frac{7}{16} & 0.125 \\ 0.125 & 0.25 \end{bmatrix}. \tag{2.19}$$

Detailed derivation of the resistivities from the Boltzmann equation under the same assumptions yields somewhat different values of the coefficients [24, 15]

$$\hat{r}_{\alpha\beta}^{rKT} = \begin{bmatrix} \frac{1}{\Psi} - 0.40044 & 0.126 \\ & \\ 0.126 & 0.2905 \end{bmatrix}, \tag{2.20}$$

in which Ψ is the condensation coefficient in this detailed model, that is usually assumed to be unity, therefore, $\hat{r}_{11}^{KT} \simeq 0.6$. The difference between the simplified model yielding (2.19) and the accurate Kinetic Theory model (2.20) lies in the omission of Knudsen layers in the former. To offset the difference in $\hat{r}_{11}$ in the less detailed model (2.19), one can set $\psi = 0.964$. While it is possible to adjust $\hat{r}_{11}^{KT}$ to match the accurate model by selecting an appropriate interface coefficient, no choice of coefficient allows $\hat{r}_{22}^{KT}$ to align with the accurate model.

Nevertheless, the simplified model describes the principal behavior of the interface quite well; its explicit nonlinear relations provide a meaningful example to study nonlinearity in force-flux relations at the interface.

Note that although the dimensionless Kinetic Theory resistivities $\hat{r}_{\alpha\beta}^{KT}$ are constants, their dimensional counterparts in (2.10) depend strongly on temperature, both directly and indirectly through the saturation pressure. Therefore, we suggest evaluating the interface coefficients through dimensionless resistivities $\hat{r}_{\alpha\beta}$ to determine whether there is a nonlinear dependence on the fluxes.

2.3 Tsuruta Model

Using molecular dynamics simulations for argon-like particles, Tsuruta et al., proposed a velocity-dependent condensation coefficient, hereafter referred to as Tsuruta condensation coefficient, expressed as

$$\theta_c = \psi \left[1 - \omega \exp\left(\frac{-c_n^2}{RT_l} \right) \right], \tag{2.21}$$

where ω is the Tsuruta coefficient and c_n is particle velocity with respect and normal to the interface. This equation indicates that faster particles traveling towards the interface have more likelihood to condense. Moreover, a lower surface temperature increases the likelihood of molecules condensing upon interface collision.

Since by definition both θ_c and ψ are defined within the range $[0,\ 1]$ and the exponential term $\exp\left(\frac{-c_n^2}{RT_l}\right)$ lies within the same ranges, it follows that the Tsuruta coefficient is also constrained between 0 and 1. Note that when $\omega = 0$, θ_c reduces to the classical condensation coefficient ψ.

By combining extended Maxwell's interface model [11, 27] with Tsuruta condensation coefficient the Tsuruta model is developed. This model derives the macroscopic conditions for mass and heat transfer across the interface [18]. The nonlinear eHKS equations can be derived based on the Tsuruta model, which results in the exceedingly long expressions shown in the appendix (B.10) and (B.13). Hence, the Tsuruta model includes the eHKS model described above.

Chapter 3

Dimensionless Formulation

These nonlinear resitivities are determined from the eHKS interface equations (2.16 and 2.17) or their Tsuruta model counterpart, (B.10 and B.13). By default, these fluxes depend on the local interface properties T_l and $p_{\text{sat}}(T_l)$. To investigate the nonlinear effect of non-equilibrium on resistivities, we eliminate this dependence by making them dimensionless.

The common factor in fluxes (2.16), (2.17) (which, also, appears in the force flux relation 2.12) is $\frac{\sqrt{2\pi R T_l}}{p_{\text{sat}}(T_l)}$; by factoring this term out, the dimensionless fluxes and forces are defined as

$$\hat{J} = \frac{\sqrt{2\pi R T_l}}{p_{\text{sat}}(T_l)} J \quad , \quad \hat{q_v} = \frac{\sqrt{2\pi R T_l}}{p_{\text{sat}}(T_l)} \frac{q_v}{R T_l} \tag{3.1}$$

Moreover, we introduce dimensionless temperature and pressure deviations as

$$T_v = T_L + \Delta T \quad \Rightarrow \quad \frac{T_v}{T_l} = 1 + \frac{\Delta T}{T_l} = 1 + \Delta \hat{T}, \tag{3.2}$$

$$p = p_{\text{sat}}(T_L) + \Delta p \quad \Rightarrow \quad \frac{p}{p_{\text{sat}}(T_l)} = 1 + \frac{\Delta p}{p_{\text{sat}}(T_l)} = 1 + \Delta \hat{p}. \tag{3.3}$$

By considering (3.1), (3.2) and (3.3) in (2.16) the dimensionless mass flux reduces to

$$\hat{J} = \frac{2\psi}{2-\psi}\left[1 - \frac{1+\Delta\hat{p}}{\sqrt{1+\Delta\hat{T}}} - \frac{1}{4\pi}\frac{\sqrt{1+\Delta\hat{T}}}{1+\Delta\hat{p}}\hat{J}^2\right]. \tag{3.4}$$

We solve the quadratic equation Eq. (3.4) for $\hat{J}$. Although this equation has two possible solutions, only one of these solutions is physically meaningful, as it must satisfy the equilibrium condition $\left(\Delta\hat{T} = 0,\ \Delta\hat{p} = 0 \to \hat{J} = 0\right)$. Therefore, the valid solution reads

$$\hat{J} = \frac{-\frac{2-\psi}{2\psi} + \sqrt{\left(\frac{2-\psi}{2\psi}\right)^2 + \frac{1}{\pi}\frac{\sqrt{1+\Delta\hat{T}}}{1+\Delta\hat{p}}\left(1 - \frac{1+\Delta\hat{p}}{\sqrt{1+\Delta\hat{T}}}\right)}}{\frac{2}{4\pi}\frac{\sqrt{1+\Delta\hat{T}}}{1+\Delta\hat{p}}}. \tag{3.5}$$

Additionally, utilizing (3.1), (3.2) and (3.3) in (2.17) the dimensionless heat flux reduces to

$$\begin{aligned}
\hat{q}_v = {} & \frac{2\psi}{2-\psi}\left(2 - \frac{5}{2}\left(1+\Delta\hat{T}\right)\right)\left[1 - \frac{1+\Delta\hat{p}}{\sqrt{1+\Delta\hat{T}}}\right] - \frac{4\psi(1-\gamma)+\gamma}{2-\psi(1-\gamma)-\gamma}\Delta\hat{T}\frac{1+\Delta\hat{p}}{\sqrt{1+\Delta\hat{T}}} \\
& + \frac{1}{4\pi}\frac{\psi(1-\gamma)+\gamma}{2-\psi(1-\gamma)-\gamma}\left[\frac{1-\psi}{2-\psi}\frac{8\gamma}{\gamma+(1-\gamma)\psi}\left(\frac{\sqrt{1+\Delta\hat{T}}}{1+\Delta\hat{p}} - \frac{7}{4}\left(\frac{\sqrt{(1+\Delta\hat{T})}^3}{1+\Delta\hat{p}}\right)\right.\right. \\
& \left.\left. + \frac{1}{2}\left(\frac{(1+\Delta\hat{T})}{1+\Delta\hat{p}}\right)^2\right) - \left(\frac{\sqrt{(1+\Delta\hat{T})}^3}{1+\Delta\hat{p}} + 2\left(\frac{(1+\Delta\hat{T})}{1+\Delta\hat{p}}\right)^2\right)\right]\hat{J}^2 \\
& + \frac{1}{8\pi^2}\frac{\psi}{2-\psi}\frac{\left(1+\Delta\hat{T}\right)^{5/2}}{(1+\Delta\hat{p})^3}\hat{J}^4.
\end{aligned} \tag{3.6}$$

correspondingly, the dimensionless force-flux relation reads

$$\begin{bmatrix} \hat{F}_J \\ \\ \hat{F}_Q \end{bmatrix} = \begin{bmatrix} -\frac{5}{2}\left[\Delta\hat{T} - \ln(1+\Delta\hat{T})\right] - \ln(1+\Delta\hat{p}) \\ \\ -\frac{\Delta\hat{T}}{1+\Delta\hat{T}} \end{bmatrix} = \begin{bmatrix} \hat{r}_{11} & \hat{r}_{12} \\ \\ \hat{r}_{21} & \hat{r}_{22} \end{bmatrix} \begin{bmatrix} \hat{J} \\ \hat{q}_v \end{bmatrix}. \tag{3.7}$$

In this dimensionless form, the eHKS equations are independent of the interface temperature T_l and saturation $p_{\text{sat}}(T_l)$. Hence, the dimensionless resistivities $\hat{r}_{\alpha\beta}$ depend only on the dimensionless fluxes $\hat{J}$ and $\hat{q}_v$ and are constant in the limit of small flows.

Chapter 4

eHKS Resistivies for the Single-Flux Case ($\hat{J} = 0$ or $\hat{q_v} = 0$)

Based on the equations described above, resistivities are determined. This procedure is simpler for the Single-Flux cases, in which either the mass flux or the vapor heat flux is zero. These settings are often used in MD simulations [2].

In evaporation/condensation scenarios ($\hat{q_v} = 0$), Eq (3.7) yields

$$\hat{r}_{11} = \frac{\hat{F}_J\left(\Delta\hat{T},\ \Delta\hat{p}\right)}{\hat{J}\left(\Delta\hat{T},\ \Delta\hat{p}\right)} \quad , \quad \hat{r}_{21} = \frac{\hat{F}_Q\left(\Delta\hat{T},\ \Delta\hat{p}\right)}{\hat{J}\left(\Delta\hat{T},\ \Delta\hat{p}\right)}. \tag{4.1}$$

Temperature and pressure jumps are connected by the requirement of zero heat flux $\hat{q_v} = 0$ in Eq (3.6). Therefore, by prescribing $\hat{J}$, $\Delta\hat{T}$ and $\Delta\hat{p}$ are determined. Then these values are used to determine $\hat{F}_J$. Finally, combining these values yields the resistivities $\hat{r}_{11}$ and $\hat{r}_{21}$.

We use the same strategy in determining heat flux scenario ($\hat{J} = 0$). In which

Eq (3.7) yields

$$\hat{r}_{12} = \frac{\hat{F}_J\left(\Delta\hat{T},\ \Delta\hat{p}\right)}{\hat{q}_v\left(\Delta\hat{T},\ \Delta\hat{p}\right)} \quad , \quad \hat{r}_{22} = \frac{\hat{F}_Q\left(\Delta\hat{T},\ \Delta\hat{p}\right)}{\hat{q}_v\left(\Delta\hat{T},\ \Delta\hat{p}\right)}. \tag{4.2}$$

Figure 4.1 showcases the relationship between the resistivities and fluxes in Single-Flux case. For all the resistivities under the Single-Flux case, whether the mass flux related resistivities $\hat{r}_{11}$ and $\hat{r}_{21}$ or the heat flux related resistivities $\hat{r}_{12}$ and $\hat{r}_{22}$, a nonlinear relation is observed.

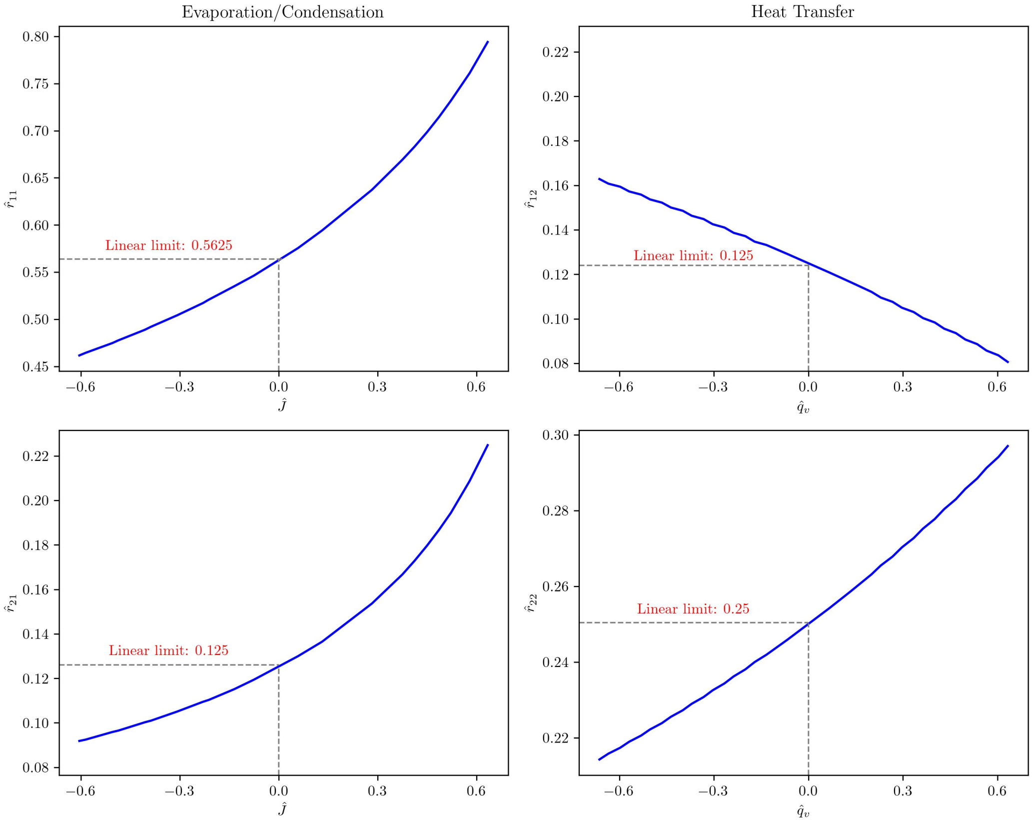

Figure 4.1: On the left, from top to bottom, $\hat{r}_{11}$ and $\hat{r}_{21}$ in the evaporation/condensation scenario for $\hat{q}_v = 0$. On the right, from top to bottom, $\hat{r}_{12}$ and $\hat{r}_{22}$ dependency in the heat transfer for $\hat{J} = 0$, for the eHKS model ($\psi = 1$ and $\gamma = 1$).

Different choices of ψ and γ shift the four resistivity plots up or down while largely preserving their nonlinear characteristics.

Notably, Onsager symmetry [28] of the off-diagonal elements is observed in the linear limit. Outside the linear limit, as the two plots are under two different types of fluxes, one can not argue symmetry or asymmetry outside the linear limit.

4.1 eHKS model vs Y/C model

The Y/C model provides a kinetic theory framework for interphase mass transfer by resolving the Knudsen layer. This layer has effects that eHKS fails to capture [26, 27]. This model is applicable only in the absence of heat transfer, making it inherently restricted. Furthermore, it assumes a condensation coefficient of unity with no variation in other coefficients.

The Hertz-Knudsen and Schrage model neglects solving the governing gas-kinetic equations for the problem, relying instead on simplified assumptions about interphase mass transfer. However, the gas-kinetic solution reveals that evaporation and condensation occur over a characteristic length scale set by the molecular mean free path, forming a Knudsen layer [26]. The equations used on deriving mass flux and determining the resistivities based on this model are explained in Appendix C.

In Fig. 4.2 Y/C model [26, 27] is plotted in black and compared against our results. The resistivity values for the eHKS model are shown by green curves. Unlike the Y/C model, The eHKS model includes heat flux scenario as well.

Since our non-linear model ignores Knudsen layers it underestimates resistivities when compared to more complete eHKS models in which Knudsen layer effects lead to larger resistance. Comparison of the curves in Fig. 4.2 shows that decreasing the condensation coefficient ψ in Eq. (3.4) to 0.964 yields good agreement with the Y/C model. However, this agreement may not hold for extreme values of $\hat{J}$, because the mass flux Eq. (3.4) used for the eHKS model is limited to the quadratic correction in $\hat{J}$ due to the approximation of the Maxwellian distribution function.

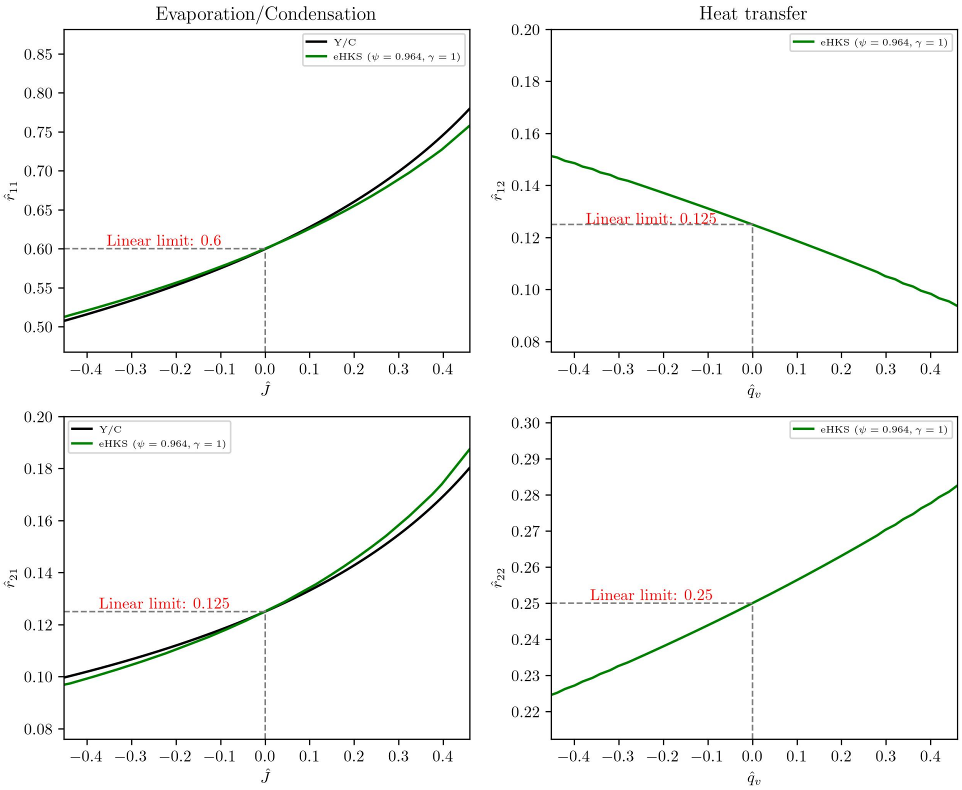

Figure 4.2: Comparison between the eHKS and Y/C models. In the eHKS model, $\psi = 0.964$ is plotted for more alignment along with ψ assumed unity. Unlike the Y/C model, The eHKS model includes heat flux scenario as well.

Chapter 5

Determining Resistivities in General Cases

5.1 Problem Statement

We now extend the determination of resistivities to a broader range of process conditions involving simultaneous heat and mass fluxes. Specifically, our goal is to obtain the dimensionless resistivities as functions of both fluxes, expressed as $\hat{r}_{\alpha\beta}\left(\hat{J},\ \hat{q}_v\right)$.

Resistivities are determined using the force-flux relation (3.7), which can be written as

$$\hat{r}_{11}\hat{J}\left(\Delta\hat{T},\ \Delta\hat{p}\right)+\hat{r}_{12}\hat{q}_v\left(\Delta\hat{T},\ \Delta\hat{p}\right)-\hat{F}_J\left(\Delta\hat{T},\ \Delta\hat{p}\right)=0, \tag{5.1}$$

$$\hat{r}_{21}\hat{J}\left(\Delta\hat{T},\ \Delta\hat{p}\right)+\hat{r}_{22}\hat{q}_v\left(\Delta\hat{T},\ \Delta\hat{p}\right)-\hat{F}_Q\left(\Delta\hat{T}\right)=0. \tag{5.2}$$

Fluxes are determined using eHKS flux expressions (3.4, 3.6) as functions of $\Delta\hat{T}$ and $\Delta\hat{p}$. Regarding forces, we use equations which are also functions of $\Delta\hat{T}$ and $\Delta\hat{p}$.

Since there are four resistivities to determine, the two governing equations (5.1) and (5.2) do not have unique solutions as soon as both fluxes, $\hat{J}$ and $\hat{q}_v$, are different from zero. Therefore, in these cases, there are infinitely many possible solutions for the nonlinear resistivities, all of which satisfy Eqs. (4.1) and (4.2) and and include the well-defined Single-Flux results from Eqs. and . Any of these solutions would correctly relate the fluxes and forces, meaning there is no definitive criterion for selecting one over the others.

Below, we present the determination of local resistivities $\hat{r}_{\alpha\beta}\left(\hat{J},\ \hat{q}_v\right)$ using an optimization procedure that considers neighboring data points to find continuous and smooth solutions close to a global initial guess, chosen here as the near-equilibrium resistivities.

When optimizing the governing equations (5.1) and (5.2), each equation is treated independently: Eq. (5.1) is used to determine $\hat{r}_{11}$ and $\hat{r}_{12}$ while Eq. (5.2) is used to determine $\hat{r}_{21}$ and $\hat{r}_{22}$. As a result, Onsager symmetry cannot be expected unless it is explicitly enforced.

Following the arguments in Ref. [10], supporting symmetry, we enforce it by setting $\hat{r}_{21} = \hat{r}_{12}$ in Eqs. (5.1) and (5.2), which yields

$$\frac{\hat{F}_J\left(\Delta\hat{T},\ \Delta\hat{p}\right) - \hat{r}_{11}\hat{J}\left(\Delta\hat{T},\ \Delta\hat{p}\right)}{\hat{q}_V\left(\Delta\hat{T},\ \Delta\hat{p}\right)} = \frac{\hat{F}_Q\left(\Delta\hat{T}\right) - \hat{r}_{22}\hat{q}_V\left(\Delta\hat{T},\ \Delta\hat{p}\right)}{\hat{J}\left(\Delta\hat{T},\ \Delta\hat{p}\right)}, \tag{5.3}$$

This relation has infinitely many local solutions for $\widehat{r}_{11}$ and $\widehat{r}_{22}$ all of which ensure symmetry. The corresponding off-diagonal resistivities are then obtained from the chosen solution as

$$\hat{r}_{21} = \hat{r}_{12} = \frac{\hat{F}_J - \hat{r}_{11}\hat{J}}{\hat{q}_V} = \frac{\hat{F}_Q - \hat{r}_{22}\hat{q}_V}{\hat{J}}. \tag{5.4}$$

The optimization procedure is explained in the next section.

5.2 Optimization

The optimization uses a large dataset of fluxes and forces, generated by prescribing dimensionless temperature and pressure values on a grid as

$$\Delta\hat{T} = \frac{i}{mn}\,, \quad \Delta\hat{p} = \frac{j}{mn} \quad (i,\ j = -n,\ n)\,, \tag{5.5}$$

The parameter m is chosen to ensure that the corresponding flux ranges encompass those typically found in the literature; making the results both comparable and applicable to experiments.

Using the grid (5.5), corresponding forces and fluxes are determined to create the array

$$D_{n\times n} = \left\langle \Delta\hat{T}^i \,|\, \Delta\hat{p}^j \,|\, \hat{F}_J^{i,j} \,|\, \hat{F}_Q^{i,j} \,|\, \hat{J}^{i,j} \,|\, \hat{q}_V^{i,j} \right\rangle_{\{i,j=-n,n\}}\,,$$

where $\hat{F}_J^{i,j} = \hat{F}_J\left(\Delta\hat{T}^i,\ \Delta\hat{p}^j\right)$, etc.

The task at hand is to determine the local values of the resistivities, either in the form

$$\hat{r}_{\alpha\beta}^{i,j} = \hat{r}_{\alpha\beta}\left(\Delta\hat{T}^i,\ \Delta\hat{p}^j\right)\,,$$

or, more preferably, as

$$\hat{r}_{\alpha\beta}^{i,j} = \hat{r}_{\alpha\beta}\left(\hat{J}^{i,j},\ \hat{q}_V^{i,j}\right)\,.$$

The Table 5.1 shows the flux ranges in the eHKS model ($\psi = 0.964$ and $\gamma = 1$) as a result of choosing $m = 3$.

We determined maximum dimensionless fluxes of Ref [2] as $\hat{J} = 0.456$ and $|\hat{q}_v| = 0.081$, hence the chosen range is sufficiently large to include these MD flux ranges, that we will study further below.

Based on the force-flux governing equations (5.1) and (5.2), we can define different objective functions for the optimization. We take the absolute values for any objective

	$\Delta\hat{T}$	$\Delta\hat{p}$	$\hat{J}$	$\hat{q}_v$	$\hat{F}_J$	$\hat{F}_Q$
Min	-0.333	-0.333	-1.479	-2.285	-0.468	-0.25
Max	0.333	0.333	0.707	1.606	0.405	0.5

Table 5.1: The ranges of fluxes, forces, and jumps for $m = 3$

function, ensuring that the minimum is always zero.

We enforce symmetry in the off-diagonal resistivities using the Eq. (5.3), the objective function is defined as

$$E_{\text{Enforced-Symmetry}}\left(\widetilde{r}_{11}, \widetilde{r}_{22}\right) = \left|\widetilde{r}_{21} - \widetilde{r}_{12}\right| = \left|\frac{\hat{F}_T - \widetilde{r}_{22}\hat{q}_V}{\hat{J}} - \frac{\hat{F}_J - \widetilde{r}_{11}\hat{J}}{\hat{q}_V}\right|. \tag{5.6}$$

The optimizer finds values (shown as $\widetilde{r}_{11}$ and $\widetilde{r}_{22}$) for $\widehat{r}_{11}$ and $\widehat{r}_{22}$, then off-diagonal resistivities $\widehat{r}_{12}$ and $\widehat{r}_{21}$ are solved using the Eq. (5.4). This approach is referred to as Enforced-Symmetry.

Alternatively, we can have two objective functions in one optimization procedure based on Eqs (5.1) and (5.2). Two objective functions can be defined as

$$E_J\left(\widetilde{r}_{11},\ \widetilde{r}_{12}\right) = \left|\hat{F}_J - \left(\widetilde{r}_{11}\hat{J} + \widetilde{r}_{12}\hat{q}_V\right)\right|, \tag{5.7}$$

$$E_Q\left(\widetilde{r}_{21},\ \widetilde{r}_{22}\right) = \left|\hat{F}_Q - \left(\widetilde{r}_{21}\hat{J} + \widetilde{r}_{22}\hat{q}_V\right)\right|. \tag{5.8}$$

Here, $\widetilde{r}_{\alpha\beta}$ is the optimized resistivity based on this approach, which is referred to as Unguided approach. This way, the determination of $\widetilde{r}_{11}$ and $\widetilde{r}_{12}$ is independent of $\widetilde{r}_{21}$ and $\widetilde{r}_{22}$, this independecy results in asymmetry in the off-diagonal coefficients.

We use an optimization algorithm from the open-source SciPy [35] package in Python, which determines the resistivities as the local minimum of the objective functions explained above. The code supports both unconstrained and constrained optimization, using algorithms like Nelder-Mead, BFGS, and Newton-CG for the former, and COBYLA, SLSQP, and trust-constr for the latter. The Broyden-Fletcher-Goldfarb-Shanno (BFGS) method, used in this problem, is a quasi-Newton optimizer that approximates Newton's method to iteratively minimize the objective function. It is efficient, well-suited for medium-sized problems, and widely adopted for its good convergence properties. More detail on the algorithm and its implementations are provided in Ref. [36].

This algorithm works best with accurate initial guesses to find continuous results surrounding the initial guess. To determine meaningful initial guess, we use the close-to-equilibrium resistivities. For the eHKS model, the corresponding resistivities are (2.18). However, more complex resistivities typically arise in the Tsuruta model when $\omega \neq 0$, leading to the general expressions (B.17), (B.18), (B.19) and (B.20) for the close-to-equilibrium resistivities as functions of microscopic coefficients.

The results found by the optimization, though not unique, exhibit properties that are either required or favorable:

1- The equilibrium limit and Single-Flux behavior are properly obtained,

2- The diagonal resistivities, $\widehat{r}_{11}$ and $\widehat{r}_{22}$, are positive, and the determinant, $\widehat{r}_{11}\widehat{r}_{22} - \widehat{r}_{12}\widehat{r}_{21}$or under symmetry $\widehat{r}_{11}\widehat{r}_{22} - \widehat{r}_{12}^2$, is also positive, ensuring that the resistivity matrix is positive definite in accordance with the second law of thermodynamics.

3- The resistivities are smooth functions of the fluxes $\hat{r}_{\alpha\beta}\left(\hat{J},\, \hat{q}_v\right)$, with no sudden jumps or discontinuity.

5.3 Equilibrium Limit Resistivities Using Optimization

As a first check of the optimization method, we consider the equilibrium limit.

The optimization process with $\psi = 0.964$ and $m = 100$ (to have all datapoints very close to equilibrium state) and 100 by 100 datapoints, using Enforced-Symmetry approach, yields the resistivity matrix for vanishing fluxes $\hat{J} \to 0$, $\hat{q_v} \to 0$ as

$$\hat{r}_{\alpha\beta} = \begin{bmatrix} 0.599998 & 0.124999 \\ \\ 0.124999 & 0.250051 \end{bmatrix}. \tag{5.9}$$

Also, using Unguided approach, with the same setting, the equilibrium limit resistivities are

$$\hat{r}_{\alpha\beta} = \begin{bmatrix} 0.6 & 0.125 \\ \\ 0.12499 & 0.250049 \end{bmatrix}. \tag{5.10}$$

Both are in agreement with the analytical result; the maximum error is 0.02%. [23, 18]. A global check of the validity of the obtained data is presented in Appendix D.

5.4 General cases

As said above, for general cases with both fluxes active at the same time, there should be infinitely many solutions. Given the specific initial guess and objective functions (based on the force-flux relation), the optimizer picks the results that are continuous and smooth functions for the resistivities $\hat{r}_{\alpha\beta}\left(\hat{J},\, \hat{q_v}\right)$. In addition to the smoothness seen in the figures, the residual errors associated with the optimized data are very small, as shown in the Appendix D.

To enhance clarity and readability, a subset of the data based on the Table. 5.1 has been selected to generate clear graphical representations.

5.4.1 Enforced-Symmetry

The Enforce-Symmetry is studied while having wide ranges for the fluxes of mass and heat. Figure 5.1 shows the resistivities as functions of mass and heat fluxes, highlighting a significant degree of nonlinearity.

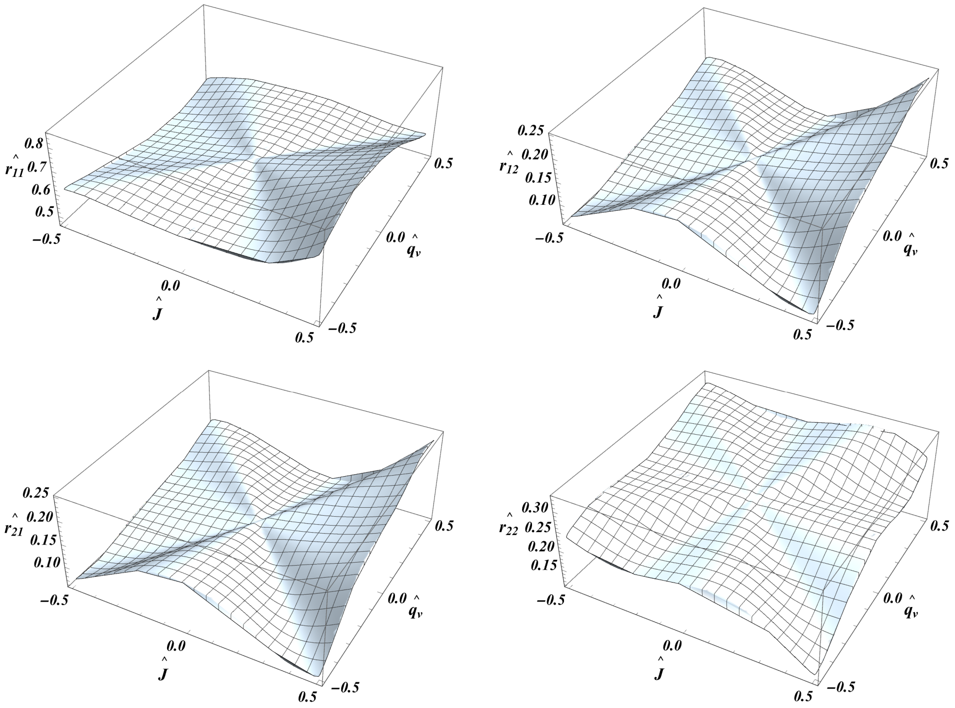

Figure 5.1: Resistivities dependence on the fluxes for the eHKS model, using Enforced-Symmetry approach; $\hat{r}_{21} = \hat{r}_{12}$, and the coefficients $\omega = 0$, $\psi = 0.964$ and $\gamma = 1$.

We emphasize again that this particular set of resistivities, Enforced-Symmetry approach, represents only one possible solution. Our main intent in presenting these results is to highlight the nonlinear behavior, which is already evident in Single-Flux scenarios and is expected to remain important in general cases.

5.4.2 Unguided

Under Unguided approach, we utilize two seperate objective functions (5.7, 5.8). This separation creates a disconnection and independency between the resistivities.

Figure 5.2 shows the resistivities as functions of mass and heat fluxes; similar to the Enforced-Symmetry general case, the degree of nonlinearity for resistivities, is remarkable.

Regarding the off-diagonal resistivities, there is difference in their behavior as a result of selection of Unguided approach. The resistivity $\hat{r}_{12}$ ranges between $-0.04 < \hat{r}_{12} < 0.22$ and exhibits stronger nonlinearity, compared to $\hat{r}_{21}$, which ranges between $0.08 < \hat{r}_{12} < 0.26$ and shows a lower degree of nonlinearity. Also, $\hat{r}_{12}$ becomes slightly negative at the extreme condition of $\hat{J} \simeq 0.7$ and $\hat{q_v} \simeq -0.7$, while the corresponding value under this condition for $\hat{r}_{21}$ is positive. This asymmetry in the off-diagonal resistivities is as a result of using Unguided approach. Nonetheless, symmetry is observed near equilibrium, with the linear limit value of 0.125.

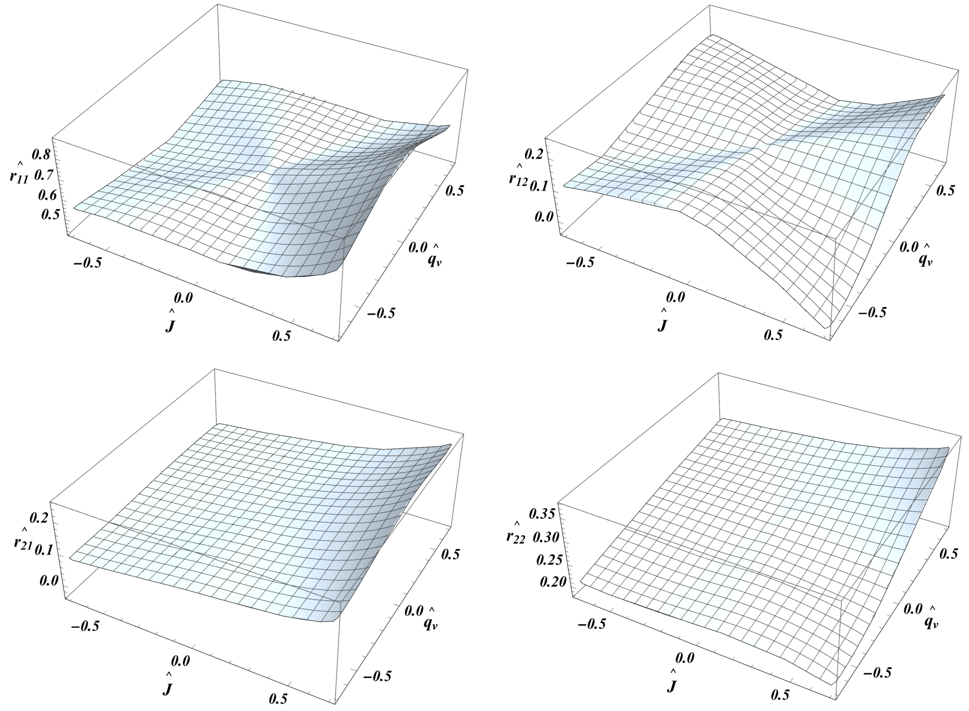

Figure 5.2: Resistivities dependence on the fluxes for the eHKS model, using Unguided approach ($\omega = 0$, $\psi = 0.964$ and $\gamma = 1$).

To expand on the asymmetry in the off-diagonal resistivity values, we consider the relative difference $\frac{\hat{r}_{21}-\hat{r}_{12}}{\hat{r}_{21}}$. As shown in Fig. 5.3, symmetry holds near equilibrium; where $\hat{r}_{12} \simeq \hat{r}_{21}$. However, asymmetry becomes evident when moving beyond the linear limits. For example, under extreme fluxes $\hat{J} \simeq 0.7$ and $\hat{q}_v \simeq -0.7$, $\hat{r}_{21}$ becomes more than two times larger than $\hat{r}_{12}$.

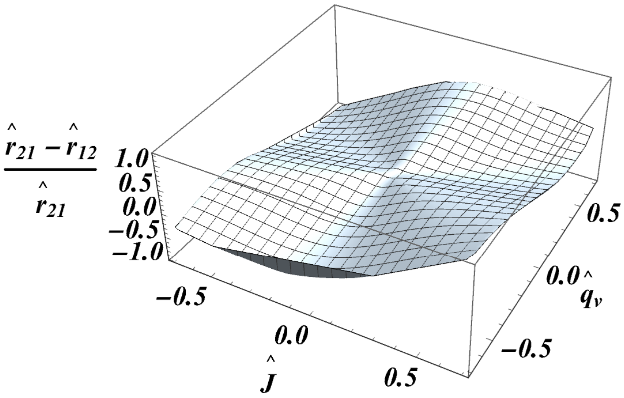

Figure 5.3: Relative difference in off-diagonal resistivities across the fluxes; Unguided approach creates asymmetry as a result of disconnecting resistivities in two objective function definitions and making them independent of each other

Chapter 6

MD Resistivities

MD simulations provide a high-resolution alternative for studying interfaces with precise control over parameters like evaporation flux and temperature gradients. These simulations require strong non-equilibrium conditions, with large evaporation fluxes and steep temperature gradients for heat transfer, to obtain data above stochastic noise [10, 19]. However, as conditions approach equilibrium, unavoidable stochastic noise effects increase, making it harder to extract meaningful transport properties. This trade-off complicates the determination of interface resistivities, as near-equilibrium simulations suffer from higher uncertainty due to the stochastic noise.

In a recent MD study [2], Homes and Vrabec used MD simulations of a simple fluid to determine interface resistivities based on Single-Flux case. They proposed that resistivities depend only on interface temperature, even under extreme conditions typical of MD.

Homes and Vrabec provided their detailed data, 44 evaporation scenarios and 36 heat transfer scenarios, with the following quantities for each scenario:

1- The bulk liquid and interface temperatures,

2- Corresponding saturation pressures,

3- The evaporation or heat transfer flux and

4- Corresponding MD resistivities.

In this and the next section, using data from Ref. [2], we examine how resistivities vary relative to interface temperatures and large non-equilibrium fluxes.

Figure 6.1 presents the MD resistivities with respect to the interface temperatures, which was found in Ref [2]. Note that this figure exhibits underlying stochastic noise, particularly for $\hat{r}_{11}$. Moreover, there is a strong dependence on temperature, which leads to a rapid decrease in the values of all four resistivities.

However, according to the Kinetic Theory of Gases, re-scaling the dimensionless approach using Eq. (2.10), helps us eliminate the temperature and, more effectively, saturation pressure effects which prevent us from clearly observing the dependence on the fluxes. Therefore, we use the MD data to determine the equivalent dimensionless resistivities based on the approach explained in Chapter 3 Eq. (2.10).

In Fig. 6.2, resistivities are dimensionless using Eq. (2.10) and shown with respect to the interface temperatures. Comparing Fig. 6.2 against Fig. 6.1, the exponential temperature dependence of the MD resistivities shown in Fig 6.1 is now taken away. Therefore, the dimensionless form makes it much easier and more compact to compare with the eHKS model. Moreover, although the asymmetry in the off-diagonal resistivities is present in both figures, it is much more pronounced and easier to observe in Fig 6.2.

Regarding the off-diagonals, in Fig 6.2, $\hat{r}_{21}$ experiences an increasing trend, mostly below 0.25, whereas, the majority of values of $\hat{r}_{12}$, appears to fluctuate above 0.25. Therefore, there is asymmetry in the off-diagonal resistivities.

Other than the off-diagonals, due to the noisy data, it is difficult to draw a clear conclusion about the resistivities' behavior based solely on temperature. However, in Fig 6.2, in general, $\hat{r}_{11}$ and $\hat{r}_{22}$ exhibit a decreasing trend.

Since resistivities are influenced by factors beyond temperature, we shift the focus

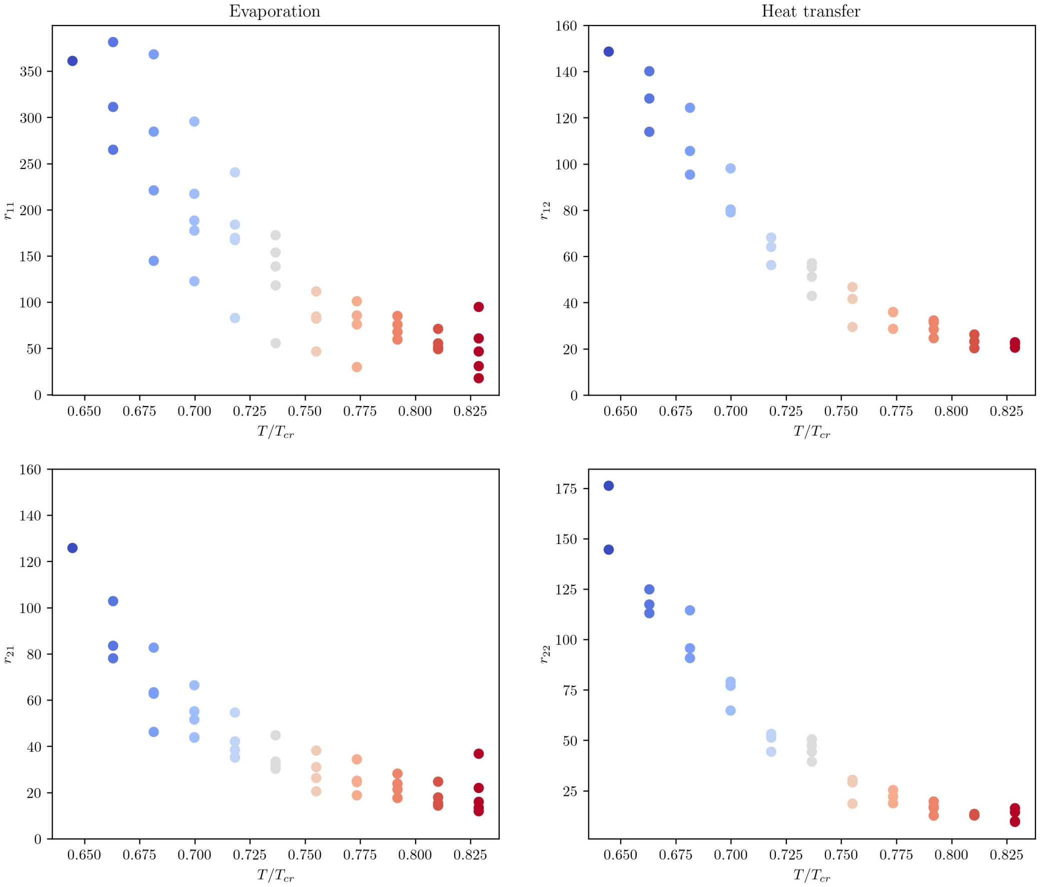
Evaporation

Heat transfer

Figure 6.1: Exponential MD points taken from Ref [2] with respect to their interface temperatures, Exponential behavior due to not eliminating $p_{\text{sat}}\left(T_l\right)$ in the unit reduction approach

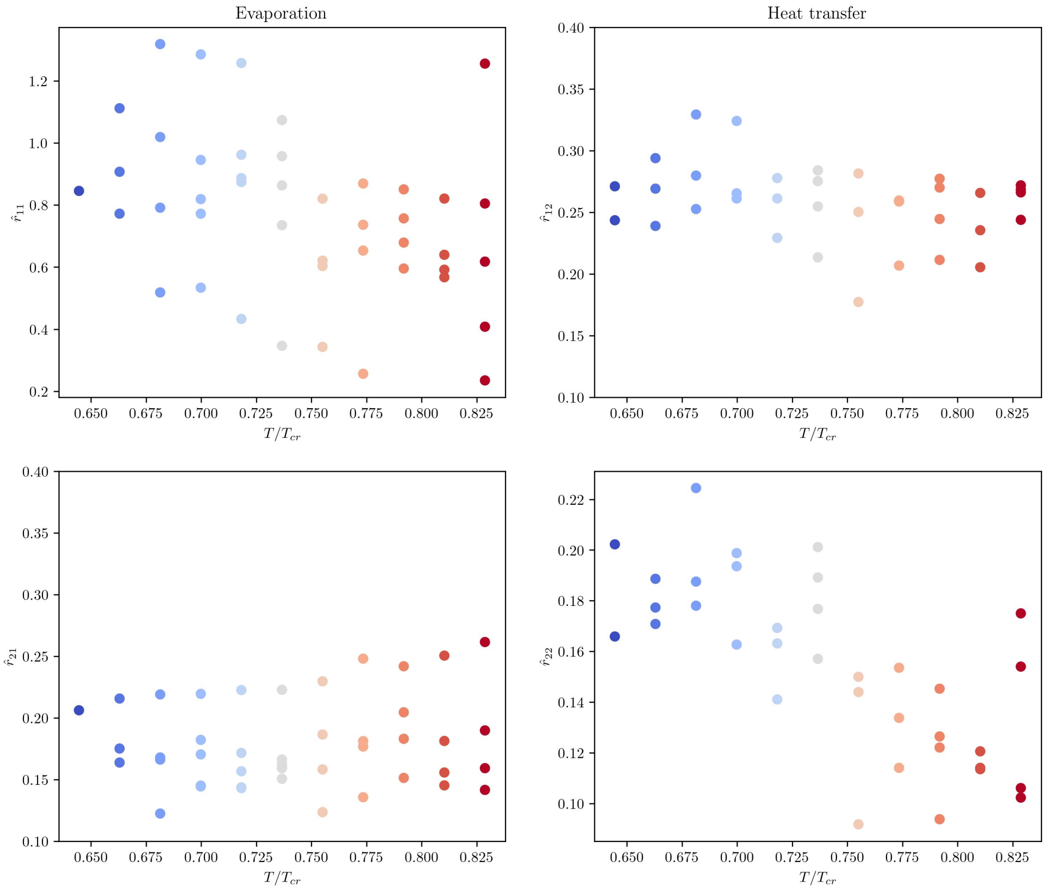

Figure 6.2: Dimensionless MD points taken from Ref [2] with respect to their interface temperatures

toward the role of fluxes in the process.

Figure 6.3 shows the resistivities with respect to fluxes and colored based on their temperature. Mass flux and heat flux are in positive and negative directions, respectively, and similar to the Single-Flux case discussed in the previous section, there is only the presence of one flux at a time. Upon broad visual inspection, the resistivities appear more structured and follow a clearer pattern when plotted against their corresponding fluxes compared to the previous figures.

For $\hat{r}_{11}$, for small values of mass flux, there is a lot of noise and not easy to draw a clear conclusion. However, at higher interface temperatures, the noise decreases. Both

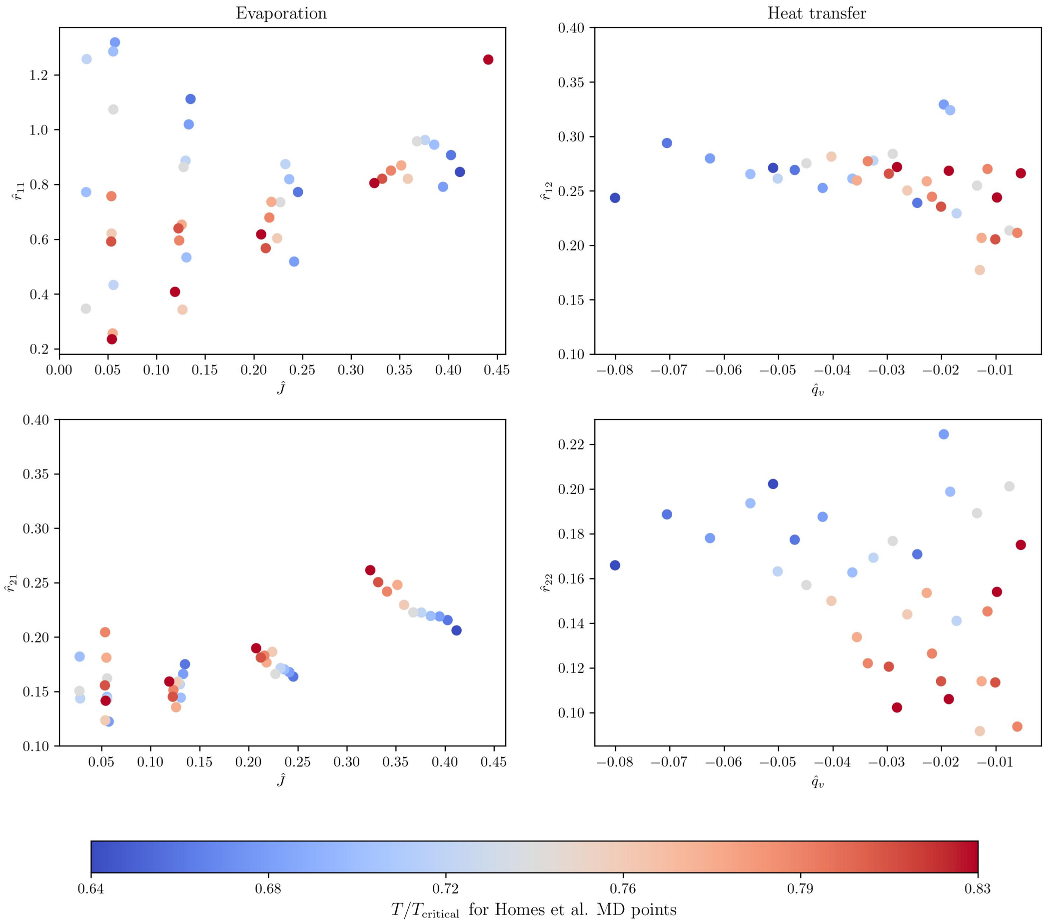

Figure 6.3: Dimensionless MD points taken from Ref [2] with respect to their fluxes and colored based on their interface temperatures

evaporation-related resistivities $\hat{r}_{11}$ and $\hat{r}_{21}$ have an overall increasing pattern with respect to the mass flux, which we have, also, seen in the eHKS and Y/C model.

For the heat-transfer related resistivities $\hat{r}_{12}$ and $\hat{r}_{22}$, it is evident higher interface temperatures are associated with less heat transfer rates and lower resistivities than at colder interface points.

These interpretations indicate an underlying cause that calls for further investigation on the topic of nonlinear relations. Similar to the previous section, the resistivites' behavior is compared with the eHKS in the next section.

6.1 eHKS Model vs MD

At temperatures sufficiently below the critical point, the vapor phase exists at relatively low densities, meaning inter-molecular forces are weak. In ideal gases, these forces are negligible, so the gas molecules move independently without significant attraction or repulsion. Therefore, to make a valid comparison, as discussed in Chapter 3, we have selected points with interface temperatures in the range of $T_{Interface} < 0.76\ T_{critical}$ ensuring they align with the ideal gas assumption and flux ranges used in this work. Resistivities and fluxes are non-dimensionalized as described in (2.10) and Chapter 3.

In Fig. 6.4 MD points [2] are shown over $\hat{J}$ and $\hat{q}_v$, and again, colored based on their interface temperatures, and compared against our results. For the sake of connecting to the previous section, Y/C model is also plotted in black. The resistivity values for the eHKS model are shown by green, purple and orange curves.

As discussed above, the green curve uses the condensation coefficient $\psi = 0.964$ to match the more refined eHKS model of Y/C, while the purple curve uses coefficients $\psi = 0.8$ and $\gamma = 0.4$ to better fit the evaporation resistivities (left column) by MD results. Furthermore, the orange curve is used to fit the heat transfer off-diagonal resistivity $\hat{r}_{12}$.

Since the MD data is not symmetric in the linear limit, while the eHKS model is symmetric (the off-diagonal resistivities are shown with colored values on the vertical axes), there is no set of coefficients within their domain $\psi,\ \gamma \in [0,\ 1]$ that best fits all four MD resistivities, therefore, matching the two appears impossible.

Nevertheless, our model reasonably predicts the behavior in $\hat{r}_{11}$ and $\hat{r}_{21}$ (both Y/C model and MD results) and, as for the heat transfer, the overall trends are relatively in alignment with the MD results [2]. This shows the model effectively captures the principle underlying the interface's behavior for studying nonlinearity in force-flux interactions.

For the off-diagonal resistivities, Onsager symmetry is obeyed in all three eHKS curves as the system approaches equilibrium, also indicated by the colored values on the vertical axes in both $\hat{r}_{12}$ and $\hat{r}_{21}$ plots.

Regarding $\hat{r}_{12}$, it has a milder behavior. This mildness can be due to the fact that there is less extremity in dimensionless heat flux compared to the dimensionless mass flux case. As discussed Single-Flux cases, larger heat flux case shown in $\hat{r}_{12}$ plot of Fig. 4.1 verifies the increasing trend (for the negative heat transfer).

Lastly, for $\hat{r}_{22}$, the same argument as $\hat{r}_{12}$ is the case, the mild decreasing trend can be pointed to the fact that the dimensionless heat flux is 8 times smaller than what is shown previously in Fig. 4.1.

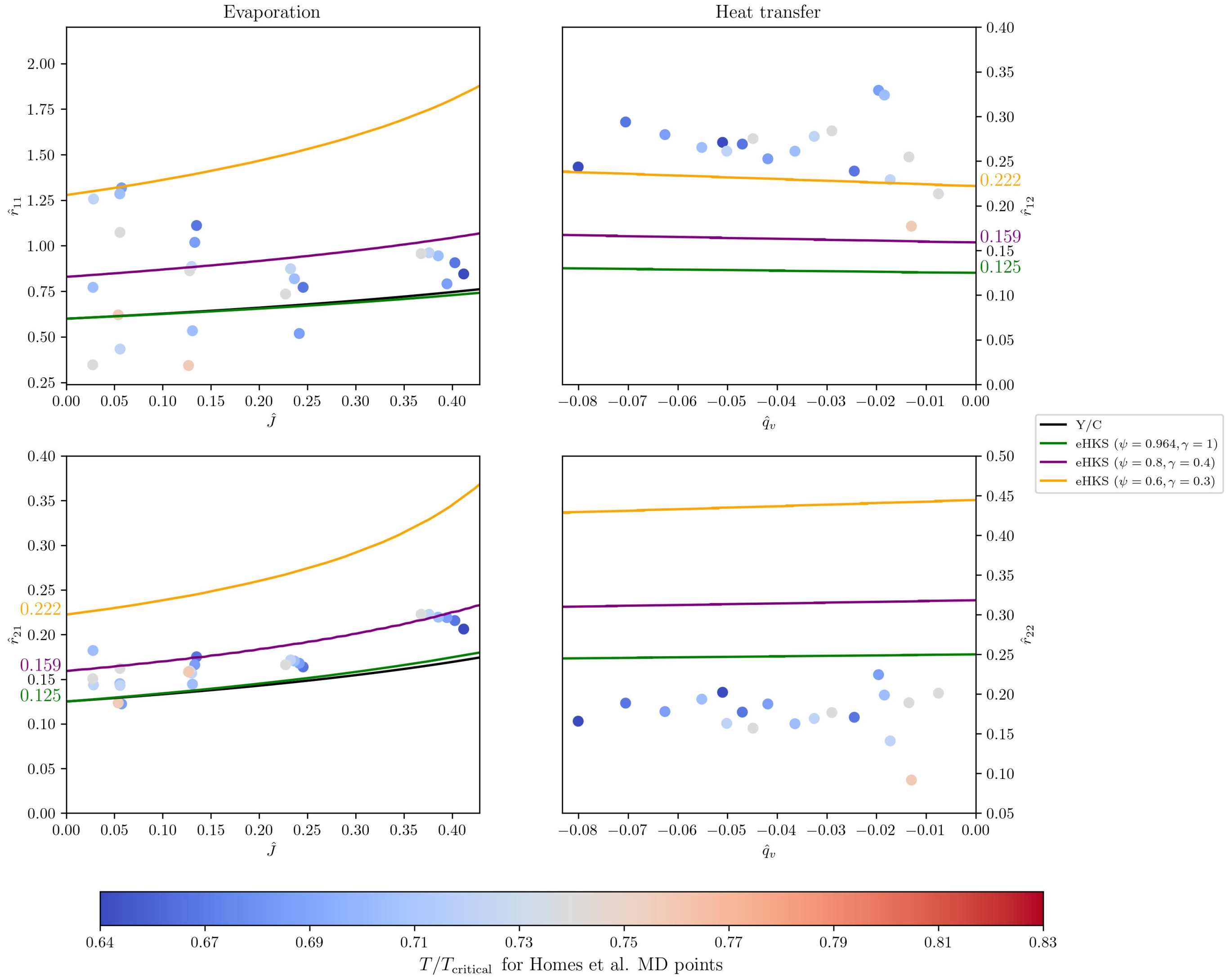

Figure 6.4: Resistivity comparison: the points represent selected data from MD simulations colored based on their interface temperature [2], the eHKS model is shown by green, purple and orange curves

Chapter 7

Tsuruta Model

To study influence of velocity dependent condensation coefficients on resitivities, we present some results for the Tsuruta model, for which the numerical determination of resistivities relies on (B.10) and (B.13). As discussed before, this model includes the eHKS model when Tsuruta coefficient ω is set to zero.

7.1 Tsuruta Coefficient Impact on Fluxes

To understand the impact of the Tsuruta coefficient ω on the fluxes and resistivities, we incrementally increase ω and observe its influence at each increment. Given that ω ranges between 0 and 1, our analysis is structured as follows:
We examine low to moderate values of ω as 0.3 and 0.5 respectively, then analyze a special value $\omega = 0.735$, which is shown below, there is a sign change in the off-diagonal resistivities. Ultimately, we study the maximum value $\omega = 1$ to encompass the entire permissible range of ω. Similar to the previous section, we set $\psi = 1$ and $\gamma = 1$.

Firstly, to demonstrate the dependence of the fluxes on ω with having the same ranges of $\Delta\hat{T}$ and $\Delta\hat{p}$ ($m = 3$ for all cases), Fig. 7.1 illustrates that as ω increases, the coverage areas of $\hat{J}$ and $\hat{q}_v$ become smaller, signifying a negative correlation between

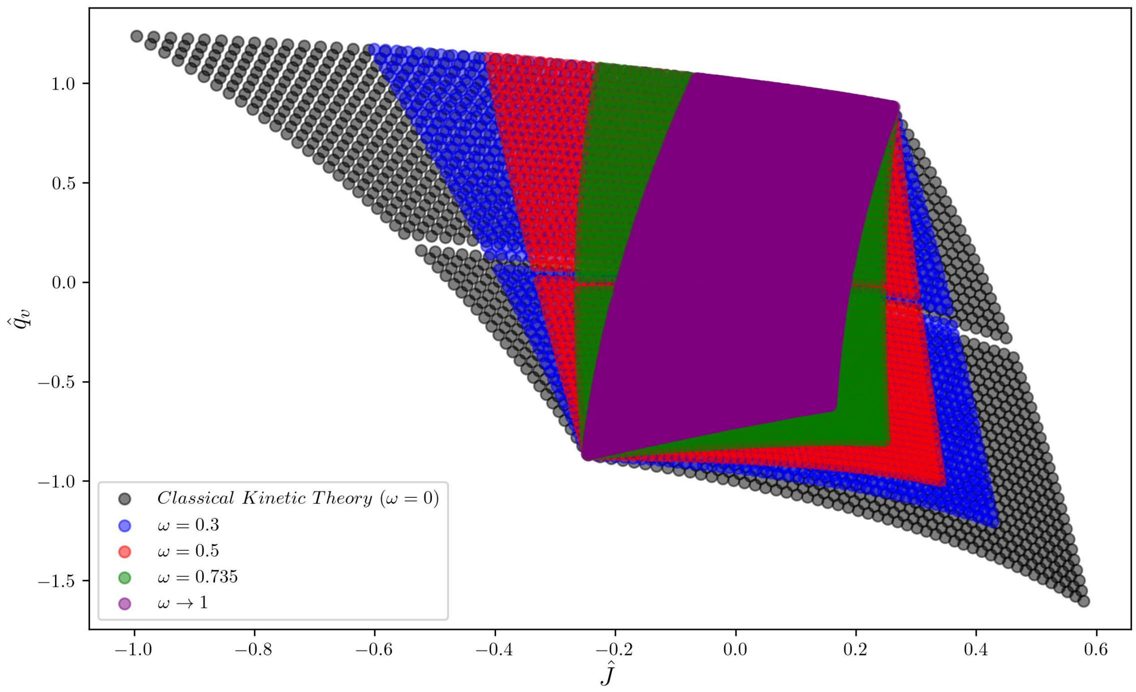

Figure 7.1: The impact of ω (ranging from 0 to 1) while keeping the same temperature and pressure ranges in mass flux (B.10) and heat flux (B.13), also, $\psi = 1$ and $\gamma = 1$.

ω and the flux magnitudes, especially the mass flux is undergone considerable decrease when increasing ω from 0.3 to 1.

Additionally, an intriguing behavior is observed when ω reaches 0.735; a curvature change occurs in the coverage areas, for $\omega \geq 0.735$ we see a reverse direction in the slopes compared to the values $\omega < 0.735$.

7.2 Resistivies for Single-Flux Case

The Single-Flux case is studied using the same method described in Chapter 4 Eqs. (4.1, 4.2). However, the fluxes are determined using the Tsurua model interface expressions (B.10) and (B.13).

Consequently, Fig. 7.2 shows the resistivities for the Single-Flux cases for the four values of omega. Close-to-equilibrium resistivities: for ω= 0.3, 0.5, 0.735 and 1, $\hat{r}_{11}$ exhibits an upward shift of 22%, 43%, 77%, and 141%, on each increment with respect to the classical Kinetic Theory resistivities (2.19).

Furthermore, $\hat{r}_{12}$ and $\hat{r}_{21}$ show a decrease of 29%, 56%, 101%, and 184% with respect to the classical Kinetic Theory resistivities (2.19). Onsager symmetry [28] is confirmed; shown by the limit values of the off-diagonal resistivities.

When $\omega = 0.735$, the off-diagonal resistivities at the linear limit $\hat{r}_{12} \simeq \hat{r}_{21} \simeq 0$. Above this value $\omega > 0.735$, a sign change to negative occurs in the off-diagonal coefficients. The negative sign in the off-diagonal resistivities in the linear limit, for $\hat{r}_{21}$, indicates that the temperature jump for the Tsuruta model with the Tsuruta coefficient above $\omega > 0.735$ has the opposite sign compared to the temperature jump in the eHKS model. Additionally, for $\hat{r}_{21}$, indicates that the pressure jump has the opposite sign compared to the pressure jump in the eHKS model.

Lastly, $\hat{r}_{22}$ shows the smallest reaction to ω, with increase shifts of 4%, 8%, 14%, and 26%, compared to the classical case.

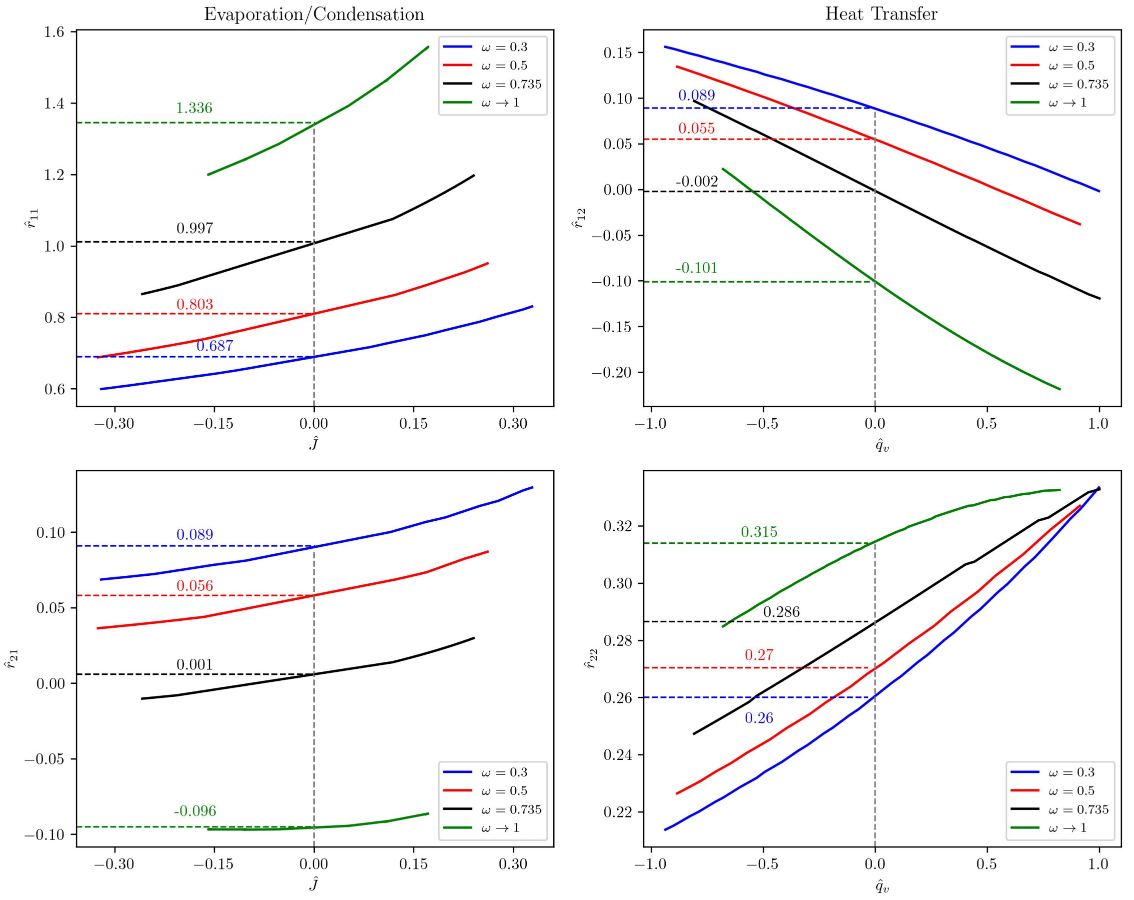

Figure 7.2: On the left, from top to bottom, $\hat{r}_{11}$ and $\hat{r}_{21}$ in the evaporation/condensation scenario. On the right, from top to bottom, $\hat{r}_{12}$ and $\hat{r}_{22}$ dependency in the heat transfer, based on four different values of ω across its range $0 \leq \omega \leq 1$, moreover, $\psi = 1$ and $\gamma = 1$.

7.3 Discussion on General Case for the Tsurua Model

Just like discussed in Chapter 5 regarding the General case for the eHKS model, due to the problem being indeterminate for General cases with both fluxes active, there are infinitely many possible solutions.

Since our main intention is to show the nonlinearity in resistivities $\hat{r}_{\alpha\beta}\left(\hat{J},\, \hat{q}_v\right)$, which we already show in previous Chapters as well as Fig. (7.2) for the Tusurua model, there will not be a valuable physical insight in creating a non-unique set of results for the Tsuruta model under the General case as that would be one of the infinitely many solutions.

Chapter 8

Conclusion and Outlook

8.1 Summary

We studied the nonlinear effects of interfacial resistivities over a wide range of non-equilibrium conditions, particularly under extreme forces and fluxes, using the extended HKS and Tsuruta models [21].

Dimensional resistivities are strongly dependent on the temperature and saturation pressure, which masks the influence of mass flux and heat flux in the process. To address this, a dimensionless formulation is used to determine resistivities. This allows us to better observe the dependence of resistivities on the fluxes beyond the effect of the temperature and saturation pressure [25].

Our results show that resistivities, which are traditionally considered functions of only interface temperature in Linear Irreversible Thermodynamics (LIT), are significantly influenced by mass and heat fluxes when the system is driven far from equilibrium. By considering Single-Flux case, i.e., vanishing mass or heat flux, we have demonstrated that resistivities exhibit a clear flux dependence, supporting previous arguments in Ref. [10].

This finding is in agreement with more refined model of Y/C for evaporation cases, i.e., vanishing heat flux. Also, our model generalizes to involve heat flux cases as well.

Regarding the General case, in which both fluxes are different from zero, due to the problem being indeterminate, there are infinitely many solutions to resistivities, i.e., there is no unique sets of solutions to the problem. However, we use an optimization method which finds continuous and smooth solutions close to a global initial guess, chosen here as the near-equilibrium resistivities. Computed resistivities based on the optimization method are one of the infinitely many valid set of solutions to the problem. These resistivities, as well, show dependecy on the fluxes.

We use the data from a recent MD study, Ref. [2], and non-dimensionalize it. It is shown that MD resistivities are, also, influenced by the fluxes. Also, MD resistivities are compared with the eHKS model; a reasonable agreement is observed, particularly for the evaporation scenario resistivities.

By incorporating the Tsuruta coefficient, we gained additional insight into utilizing the velocity-dependent condensation coefficient [21]. Our results show that this model significantly impacts resistivities, both for non-equilibrium and linear limit conditions. Additionally, we found that selecting a Tsuruta coefficient of $\omega > 0.735$ (keeping $\psi = 1$ and $\gamma = 1$) yields negative resistivities for close to equilibrium limit, which implies an opposite sign in the temperature and pressure jumps compared to those predicted by the eHKS model.

The Tsuruta model, compared to the eHKS, provides the additional Tsuruta coefficient ω, offering more flexibility in fitting experimental data. However, , unlike both eHKS and Tsurua models, the MD data in Ref. [2] exhibits asymmetry in the linear limit. Therefore, there is no set of coefficients within the domain $\psi,\ \gamma,\ \omega \in (0,\ 1)$ that can simultaneously fit all four MD resistivities.

8.2 Future Work

To further investigate the nonlinearity of interfacial resistivities, future research should prioritize conducting both physical and simulation-based experiments with higher accuracy and reliability. Physical experiments remain essential for establishing reliable interfacial models. Improved measurement techniques, particularly for capturing temperature and pressure jumps with minimal error, will be beneficial in improving our understanding of resistivity behavior in non-equilibrium conditions.

Molecular Dynamics (MD) simulations have provided valuable insight into interfacial transport by capturing atomistic-scale interactions. However, their results must be interpreted cautiously due to inherent stochastic noise. More MD studies, with larger system sizes to enhance statistical sampling and reduce fluctuations, as well as, longer simulation time scales to avoid transient effects, are necessary to reduce stochastic noise and provide a more reliable reference for comparison with theoretical models.

We used an extended Hertz-Knudsen-Schrage nonlinear kinetic theory model that includes heat transfer expression. While this model shows reasonable agreement with the Y/C model in the specific case of evaporation [27], it is inherently simplified due to the omission of Knudsen layer contributions. Enhancing this model to account for the Knudsen layer would be a valuable improvement.

Moving forward, our research will aim to generalize the analysis by accounting for real gas effects. This requires moving beyond the ideal gas assumption and adopting more complex model that accounts for intermolecular forces and deviations from the ideal equation of state. Incorporating real gas behavior improves the accuracy of resistivity determinations, particularly for high-density vapors and near-critical conditions where the ideal gas assumption breaks down.

Appendix A

Simplification of the Force-Flux Relation

In this appendix, we show the simplification of the thermodynamic force for mass flux for the model considering ideal gas and incompressible liquid. The thermodynamic force for mass flux in (2.8) reads

$$F_J = \frac{g_l}{T_l} - \frac{g_v}{T_v} + h_v \left(\frac{1}{T_v} - \frac{1}{T_l} \right) . \tag{A.1}$$

the Gibbs free energy of the liquid $g_l = g_l \left(T_l, \ p \right)$ can be rewritten as $g_l \left(T_l, \ p_{\text{sat}}(T_l) + \Delta p \right)$, where pressure deviation for the liquid phase is defined as $\Delta p = p - p_{\text{sat}}(T_l)$. Taylor expansion in pressure yields

$$g_l \left(T_l, \ p_{\text{sat}} \left(T_l \right) + \Delta p \right) = g_l \left(T_l, \ p_{\text{sat}} \left(T_l \right) \right) + \left(\frac{\partial g_l}{\partial p} \right)_{T_l, p_{\text{sat}}(T_l)} \Delta p + \left(\frac{\partial^2 g_l}{\partial p^2} \right)_{T_l, p_{\text{sat}}(T_l)} \Delta p^2 + \dots . \tag{A.2}$$

From the Gibbs equation follows the thermodynamic property relation [37],

$$\left(\frac{\partial g_l}{\partial p} \right)_{T_l, p_{\text{sat}}(T_l)} = \nu_l \left(T_l, p_{\text{sat}} \left(T_l \right) \right) = \nu_l^{\text{sat}} \left(T_l \right) , \tag{A.3}$$

where ν_l is the specific volume of the liquid phase, which we consider incompressible liquid and approximate independent of pressure; thus higher expansion terms in (A.2) vanish, so that

$$g_l\left(T_l,\ p\right) = g_v^{\text{sat}}\left(T_l\right) + RT_l \frac{\nu_l^{\text{sat}}\left(T_l\right)}{\nu_v^{\text{sat}}\left(T_l\right)} \frac{\Delta p}{p_{\text{sat}}\left(T_l\right)}, \tag{A.4}$$

where we have used the equilibrium condition $g_v^{\text{sat}}\left(T_l\right) = g_l^{\text{sat}}\left(T_l\right)$ and the ideal gas law as $\frac{p_{\text{sat}}(T_l)}{RT_l} = \frac{1}{\nu_v^{\text{sat}}(T_l)}$.

Inserting in (A.4), together with $g = h - Ts$ yields

$$F_J = \frac{h_v^{\text{sat}}\left(T_l\right) - h_v\left(T_v\right)}{T_l} + s_v\left(T_v,\ p\right) - s_v^{\text{sat}}\left(T_l\right) + R \frac{\nu_l^{\text{sat}}\left(T_l\right)}{\nu_v^{\text{sat}}\left(T_l\right)} \frac{\Delta p}{p_{\text{sat}}\left(T_l\right)} \tag{A.5}$$

Applying monatomic ideal gas property relations

$$h_v^{\text{sat}}\left(T_l\right) - h_v\left(T_v\right) = \frac{5}{2} R\left(T_l - T_v\right), \tag{A.6}$$

and

$$s_v\left(T_v,\ p_v\right) \text{-} s_v^{\text{sat}}\left(T_l\right) = R\left(\frac{5}{2} \ln \frac{T_v}{T_l} - \ln\left(1 + \frac{\Delta p}{p_{\text{sat}}\left(T_l\right)}\right)\right), \tag{A.7}$$

in Eq. (A.5), we derive the form

$$F_J = R\left(\frac{5}{2} \frac{\left(T_l - T_v\right)}{T_l} + \ln \frac{T_v}{T_l} - \left[\ln\left(1 + \frac{\Delta p}{p_{\text{sat}}\left(T_l\right)}\right) - \frac{\nu_l^{\text{sat}}\left(T_l\right)}{\nu_v^{\text{sat}}\left(T_l\right)} \frac{\Delta p}{p_{\text{sat}}\left(T_l\right)}\right]\right). \tag{A.8}$$

In this equation, the term in the square brackets can be further simplified. Using Taylor expansion, the term $\ln\left(1 + \frac{\Delta p}{p_{\text{sat}}(T_l)}\right) \simeq \frac{\Delta p}{p_{\text{sat}}(T_l)}$, therefore, this term becomes

$$\frac{\Delta p}{p_{\text{sat}}\left(T_l\right)} \left(1 - \frac{\nu_l^{\text{sat}}\left(T_l\right)}{\nu_v^{\text{sat}}\left(T_l\right)}\right). \tag{A.9}$$

Since specific volume for vapor is much larger than that for liquid the fraction $\frac{\nu_l^{\text{sat}}(T_l)}{\nu_v^{\text{sat}}(T_l)} \ll 1$, hence, can be ignored. The final simplified form yields

$$F_J = R\left(\frac{5}{2}\frac{T_l - T_v}{T_l} + \ln\frac{T_v}{T_l} - \ln\frac{p}{p_{\text{sat}}\left(T_l\right)}\right). \tag{A.10}$$

Appendix B

Kinetic Theory and Tsuruta Interface Models

In Ref. [18], the detail of the kinetic model is discussed, which combines Maxwell's classical interface model [27, 11] with a velocity based condensation coefficient [21].

The only difference in contrast to what is done in Ref [18] is that we consider higher order terms in the expansion to approximate the Maxwellian distribution function.

The Chapman-Enskog (CE) expansion approximates the distribution function by expanding it in terms of the Knudsen number (Kn), as derived from the Boltzmann equation. For the evaporation problems considered in this study, shear stresses can be neglected [23]. Under this assumption, the first-order CE expansion yields the distribution function [11]

$$f_{CE} = f_M\left(p, RT, c\right)\left\{1 + \frac{c_x j}{p} + \frac{1}{2}\frac{j^2}{p^2}\left(c_x^2 - RT\right) + \frac{1}{6}\frac{j^3}{p^3}c_x\left(c_x^2 - 3RT\right) + \frac{2}{5}\frac{qc_x}{pRT^2}\left(\frac{c^2}{2} - \frac{5}{2}RT\right)\right\}, \tag{B.1}$$

where $f_M\left(p, RT, c\right)$ and c_x are Maxwellian distribution function and particle velocity in 1-D, respectively. It is convenient to choose the frame of reference such that the evaporating interface is at rest [18, 23].

Using distribution function in Eq. (B.1), we can compute the bulk properties. The mass density reads

$$\rho = \frac{p}{RT} = m \int f_{CE} \, d\mathbf{c}, \tag{B.2}$$

here, m denote as particle mass.
Mass flux J reads

$$\rho v = J = m \int c_x f_{CE} \, d\mathbf{c}. \tag{B.3}$$

By ignoring the shear stresses in the 1-D geometry, momentum flux reads

$$p + \rho v^2 = p + \frac{RT}{p} j^2 = m \int c_x^2 f_{CE} \, d\mathbf{c}. \tag{B.4}$$

The total energy density, expressed as the sum of internal energy density and kinetic energy density, reads

$$\rho \left(\frac{3}{2} RT + \frac{v^2}{2} \right) = \frac{3}{2} p + \frac{1}{2} \frac{RT}{p} j^2 = m \int \frac{1}{2} c^2 f_{CE} \, d\mathbf{c}. \tag{B.5}$$

Energy flux Q reads

$$Q = \rho \left(\frac{5}{2} RT + \frac{v^2}{2} \right) v + q = \left(\frac{5}{2} RT + \frac{1}{2} \frac{RT}{p^2} j^2 \right) j + q = m \int \frac{1}{2} c^2 c_x f_{CE} \, d\mathbf{c}. \tag{B.6}$$

Reshaping Eq B.6, yields

$$q + \frac{1}{2} \frac{RT}{p^2} j^3 = m \int \left(\frac{1}{2} c^2 c_x - \frac{5}{2} RT \right) c_x f_{CE} \, d\mathbf{c}, \tag{B.7}$$

which helps us compute the heat flux.

The distribution in Eq. (B.1) is used to compute interface conditions for condensing and evaporating interfaces. Note that, this approach simplifies the actual physical conditions by neglecting Knudsen layer near the interface [27]. While this introduces a minor error in the analysis, the results remain valid and reliable.

For the sake of saving space and having a more compact notation, the dimensionless temperature and pressure are defined as

$$\tau = \frac{T_v}{T_l} = 1 + \Delta\hat{T}, \tag{B.8}$$

$$\Pi = \frac{p}{p_{\text{sat}}\left(T_l\right)} = 1 + \Delta\hat{p}. \tag{B.9}$$

Based on the unit reduction approach discussed in Section III Eq (3.1), this model computes the dimensionless fluxes across the interface.

As these fluxes are long polynomials, we try to have them as compact as possible. Hence, the compact mass flux reads

$$\hat{J} = \frac{\hat{J}_{\text{Numerator}}}{\hat{J}_{\text{Denominator}}}, \tag{B.10}$$

which is a function of $\hat{J}_{\text{Numerator}}$

$$
\begin{aligned}
\hat{J}_{\text{Numerator}} = 3\omega\Bigg(& -3J^2\tau^2(\psi(\omega-2)+2)(\tau+1)^3 + 4\pi\Pi^2\tau(\psi(\omega-2)+2)(\tau+1)^3 \\
& + 2\pi\Pi\sqrt{\tau}\psi(\psi(\omega-2)+2)(5\tau(\omega-2)-3\omega+8)(\tau+1)^3 \\
& + 4\pi\gamma\Pi^2(-\psi\tau+\tau+\psi(\omega-1)+1) \\
& \quad \times(-5\tau(\psi(\omega-2)+2)+\psi(3\omega-8)+8)(\tau+1)^2 \\
& + J^2\gamma\tau\Big(-(\psi-1)\tau^2-\psi(\omega+2)\tau+2\tau+\psi(\omega-1)+1\Big) \\
& \quad \times(-5\tau(\psi(\omega-2)+2)+\psi(3\omega-8)+8)(\tau+1) \\
& - 4\pi(1-\gamma)\Pi^2\tau(\psi(\omega-2)+2) \\
& \quad \times\Big(-(\psi-1)\tau^2+(\psi(3\omega-2)+2)\tau+\psi(\omega-1)+1\Big)(\tau+1) \\
& - J^2(1-\gamma)\tau^2(\psi(\omega-2)+2) \\
& \quad \times\Big(3(\psi-1)\tau^3-3(\psi(\omega-3)+3)\tau^2+(\psi(2\omega+9)-9)\tau-3\psi(\omega-1)-3\Big)\Bigg)\tau^{3/2} \\
& + \Bigg(-\tau\sqrt{\tau+1}\Big(\tau^2+(\omega+2)\tau-\omega+1\Big)J^2-4\pi\Pi^2(\tau+1)^{3/2}(\tau-\omega+1) \\
& - 2\pi\Pi\Big(\sqrt{\tau(\tau+1)}+2\sqrt{\tau^3(\tau+1)}+\sqrt{\tau^5(\tau+1)}\Big)(\omega-2)\Bigg) \\
& \times\Bigg(10\tau^{3/2}(\psi(\omega-2)+2)(\tau+1)^3-3\gamma\tau^{3/2}\psi\omega(-5\tau(\psi(\omega-2)+2) \\
& \quad +\psi(3\omega-8)+8)\sqrt{\tau+1}+(1-\gamma)\tau\sqrt{\frac{\tau}{\tau+1}}(\psi(\omega-2)+2) \\
& \quad \times\Big(-10\sqrt{\tau+1}(\psi-1)\tau^3+(13\omega\psi-30\sqrt{\tau+1}\psi+30\sqrt{\tau+1})\tau^2 \\
& \quad +(8\omega\psi-30\sqrt{\tau+1}\psi+30\sqrt{\tau+1})\tau+10\psi(\omega-\sqrt{\tau+1}) \\
& \quad +10\sqrt{\tau+1}\Big)\Bigg), \qquad \text{(B.11)}
\end{aligned}
$$

and $\hat{J}_{\text{Denominator}}$

$$
\begin{aligned}
\hat{J}_{\text{Denominator}} = 3\psi\omega\Bigg(& 2J^2\tau^{5/2}(\psi(\omega-2)+2)(\tau+1)^3 - 4\pi\gamma\Pi^2\Big((\psi-1)\tau^{5/2}+2(\psi-1)\tau^{3/2} \\
&+ (\psi-1)\sqrt{\tau} - \sqrt{\tau(\tau+1)}\psi\omega\Big)(-5\tau(\psi(\omega-2)+2)+\psi(3\omega-8)+8)(\tau+1) \\
&+ 12\pi(\gamma-1)\Pi^2\tau^{5/2}\psi(\psi(\omega-2)+2)\omega\sqrt{\tau+1} \\
&- J^2\gamma\tau^{5/2}\psi\omega(-5\tau(\psi(\omega-2)+2)+\psi(3\omega-8)+8)\sqrt{\tau+1} \\
&+ \frac{J^2(\gamma-1)\tau^{5/2}(\psi(\omega-2)+2)}{\sqrt{\tau+1}}\Big(2\sqrt{\tau+1}(\psi-1)\tau^3+(-3\omega\psi+6\sqrt{\tau+1}\psi-6\sqrt{\tau+1})\tau^2 \\
&+ 6\sqrt{\tau+1}(\psi-1)\tau + 2\psi(\sqrt{\tau+1}-\omega) - 2\sqrt{\tau+1}\Big)\Bigg)\tau^{3/2} \\
&+ \Bigg(-J^2\psi\omega\tau^{5/2}+8\pi\Pi^2(\tau+1)^{5/2}\sqrt{\tau} \\
&- 4\pi\Pi^2\psi\Big(-\omega\tau^{3/2}+2\sqrt{\tau(\tau+1)}\tau-\omega\sqrt{\tau}+\sqrt{\tau(\tau+1)}+\sqrt{\tau^5(\tau+1)}\Big)\Bigg) \\
&\times\Bigg(10\tau^{3/2}(\psi(\omega-2)+2)(\tau+1)^3-3\gamma\tau^{3/2}\psi\omega(-5\tau(\psi(\omega-2)+2) \\
&\quad+\psi(3\omega-8)+8)\sqrt{\tau+1}+(1-\gamma)\tau\sqrt{\frac{\tau}{\tau+1}}(\psi(\omega-2)+2) \\
&\quad\times\Big(-10\sqrt{\tau+1}(\psi-1)\tau^3+(13\omega\psi-30\sqrt{\tau+1}\psi+30\sqrt{\tau+1})\tau^2 \\
&\quad+(8\omega\psi-30\sqrt{\tau+1}\psi+30\sqrt{\tau+1})\tau+10\psi(\omega-\sqrt{\tau+1}) \\
&\quad+10\sqrt{\tau+1}\Big)\Bigg).
\end{aligned}
\tag{B.12}
$$

Similarly, the compact heat flux reads

$$
\hat{q}_v = \hat{q}_{v1} + \frac{\hat{q}_{v\,\text{Numerator}}}{\hat{q}_{v\,\text{Denominator}}},
\tag{B.13}
$$

which is a function of $\hat{q}_{v1}$

$$\hat{q}_{v1} = \frac{1}{6\pi\sqrt{\tau}\omega}5\left(\frac{\tau\sqrt{\tau+1}\left(\tau^2+(\omega+2)\tau-\omega+1\right)J^2}{\Pi}+4\pi\Pi(\tau+1)^{3/2}(\tau-\omega+1)+\right.$$
$$\left.2\pi\left(\sqrt{\tau(\tau+1)}+2\sqrt{\tau^3(\tau+1)}+\sqrt{\tau^5(\tau+1)}\right)(\omega-2)\right), \quad \text{(B.14)}$$

and $\hat{q}_{v\,\mathrm{Numerator}}$

$$
\begin{aligned}
\hat{q}_{v\,\mathrm{Numerator}} = {} & \sqrt{\tau}\Bigg(-4\pi(\tau+1)\Big(\tau\sqrt{\tau+1}(\psi-2)+\psi(\sqrt{\tau+1}-\omega)-2\sqrt{\tau+1}\Big)\Pi^2 - J^2\tau^2\psi\omega\Bigg) \\
& \times \Bigg(3\omega\Bigg(-3J^2\tau^2(\psi(\omega-2)+2)(\tau+1)^3+4\pi\Pi^2\tau(\psi(\omega-2)+2)(\tau+1)^3 \\
& +2\pi\Pi\sqrt{\tau}\psi(\psi(\omega-2)+2)(5\tau(\omega-2)-3\omega+8)(\tau+1)^3 \\
& +4\pi\gamma\Pi^2(-\psi\tau+\tau+\psi(\omega-1)+1) \\
& \quad \times(-5\tau(\psi(\omega-2)+2)+\psi(3\omega-8)+8)(\tau+1)^2 \\
& +J^2\gamma\tau\Big(-(\psi-1)\tau^2-\psi(\omega+2)\tau+2\tau+\psi(\omega-1)+1\Big) \\
& \quad \times(-5\tau(\psi(\omega-2)+2)+\psi(3\omega-8)+8)(\tau+1) \\
& -4\pi(1-\gamma)\Pi^2\tau(\psi(\omega-2)+2) \\
& \quad \times\Big(-(\psi-1)\tau^2+(\psi(3\omega-2)+2)\tau+\psi(\omega-1)+1\Big)(\tau+1) \\
& -J^2(1-\gamma)\tau^2(\psi(\omega-2)+2) \\
& \quad \times\Big(3(\psi-1)\tau^3-3(\psi(\omega-3)+3)\tau^2+(\psi(2\omega+9)-9)\tau-3\psi(\omega-1)-3\Big)\Bigg)\tau^{3/2} \\
& +\Bigg(-\tau\sqrt{\tau+1}\Big(\tau^2+(\omega+2)\tau-\omega+1\Big)J^2-4\pi\Pi^2(\tau+1)^{3/2}(\tau-\omega+1) \\
& -2\pi\Pi\Big(\sqrt{\tau(\tau+1)}+2\sqrt{\tau^3(\tau+1)}+\sqrt{\tau^5(\tau+1)}\Big)(\omega-2)\Bigg) \\
& \times\Bigg(10\tau^{3/2}(\psi(\omega-2)+2)(\tau+1)^3-3\gamma\tau^{3/2}\psi\omega(-5\tau(\psi(\omega-2)+2) \\
& \quad +\psi(3\omega-8)+8)\sqrt{\tau+1}+(1-\gamma)\tau\sqrt{\frac{\tau}{\tau+1}}(\psi(\omega-2)+2) \\
& \quad \times\Big(-10\sqrt{\tau+1}(\psi-1)\tau^3+(13\omega\psi-30\sqrt{\tau+1}\psi+30\sqrt{\tau+1})\tau^2 \\
& \quad +(8\omega\psi-30\sqrt{\tau+1}\psi+30\sqrt{\tau+1})\tau+10\psi(\omega-\sqrt{\tau+1}) \\
& \quad +10\sqrt{\tau+1}\Big)\Bigg),
\end{aligned}
\tag{B.15}
$$

and $\hat{q}_{v\,\text{Denominator}}$

$$
\begin{aligned}
\hat{q}_{v\,\text{Denominator}} = \Pi\Bigg(3\psi\omega\Bigg(&2J^2\tau^{5/2}(\psi(\omega-2)+2)(\tau+1)^3 \\
&- 4\pi\gamma\Pi^2\Big((\psi-1)\tau^{5/2}+2(\psi-1)\tau^{3/2}+(\psi-1)\sqrt{\tau}-\sqrt{\tau(\tau+1)}\psi\omega\Big) \\
&\quad\times(-5\tau(\psi(\omega-2)+2)+\psi(3\omega-8)+8)(\tau+1) \\
&+ 12\pi(\gamma-1)\Pi^2\tau^{5/2}\psi(\psi(\omega-2)+2)\omega\sqrt{\tau+1} \\
&- J^2\gamma\tau^{5/2}\psi\omega(-5\tau(\psi(\omega-2)+2)+\psi(3\omega-8)+8)\sqrt{\tau+1} \\
&+ \frac{J^2(\gamma-1)\tau^{5/2}(\psi(\omega-2)+2)}{\sqrt{\tau+1}}\Big(2\sqrt{\tau+1}(\psi-1)\tau^3 \\
&\quad+(-3\omega\psi+6\sqrt{\tau+1}\psi-6\sqrt{\tau+1})\tau^2+6\sqrt{\tau+1}(\psi-1)\tau \\
&\quad+2\psi(\sqrt{\tau+1}-\omega)-2\sqrt{\tau+1}\Big)\Bigg)\tau^{3/2} \\
&+\Bigg(-J^2\psi\omega\tau^{5/2}+8\pi\Pi^2(\tau+1)^{5/2}\sqrt{\tau} \\
&-4\pi\Pi^2\psi\Big(-\omega\tau^{3/2}+2\sqrt{\tau(\tau+1)}\tau-\omega\sqrt{\tau}+\sqrt{\tau(\tau+1)}+\sqrt{\tau^5(\tau+1)}\Big)\Bigg) \\
&\times\Bigg(10\tau^{3/2}(\psi(\omega-2)+2)(\tau+1)^3-3\gamma\tau^{3/2}\psi\omega(-5\tau(\psi(\omega-2)+2) \\
&\quad+\psi(3\omega-8)+8)\sqrt{\tau+1}+(1-\gamma)\tau\sqrt{\frac{\tau}{\tau+1}}(\psi(\omega-2)+2) \\
&\quad\times\Big(-10\sqrt{\tau+1}(\psi-1)\tau^3+(13\omega\psi-30\sqrt{\tau+1}\psi+30\sqrt{\tau+1})\tau^2 \\
&\quad+(8\omega\psi-30\sqrt{\tau+1}\psi+30\sqrt{\tau+1})\tau+10\psi(\omega-\sqrt{\tau+1}) \\
&\quad+10\sqrt{\tau+1}\Big)\Bigg).
\end{aligned}
\tag{B.16}
$$

Close-to-equilibrium resistivities can be determined in the limits, these resistivity expressions in Ref. [18] contained some typographical errors, the proper results read

$$\begin{aligned}\hat{r}_{11} =&\zeta \Big(\gamma \Big(-128\sqrt{2} + \psi \Big(8\sqrt{2}(41 + \psi(-34 + 9\psi)) - 2(-1 + \psi)(-16 - 60\sqrt{2}+ \\ &15\psi + 36\sqrt{2}\psi)\omega + \psi(-26 - 28\sqrt{2} + 9(3 + 2\sqrt{2})\psi)\omega^2 - 6\psi^2\omega^3\Big)\Big) \\ &+3\psi(2 + \psi(-2 + \omega))\Big(12\sqrt{2}(-2 + \omega) + \psi\Big(12\sqrt{2} + \omega(-5 - 6\sqrt{2} + 2\omega)\Big)\Big)\Big),\end{aligned} \tag{B.17}$$

$$\begin{aligned}\hat{r}_{12} =&\frac{\zeta}{10} \Big(\gamma \Big(160\sqrt{2}(-1 + \psi)^2 - 2(-1 + \psi)(48 - 80\sqrt{2}+ \\ &(-23 + 120\sqrt{2})\psi)\omega + \psi(34 - 80\sqrt{2} + 5(-3 + 16\sqrt{2})\psi)\omega^2 - 4\psi^2\omega^3\Big) \\ &+(2 + \psi(-2 + \omega))\Big(160\sqrt{2}(-1 + \omega) + \psi\Big(80\sqrt{2} + \omega(23 - 80\sqrt{2} + 4\omega)\Big)\Big)\Big),\end{aligned} \tag{B.18}$$

$$\begin{aligned}\hat{r}_{21} =&\zeta \Big(-\gamma(-2 + \omega)\Big(8\sqrt{2} + \psi\Big(8\sqrt{2}(-2 + \psi) + (2 - 8\sqrt{2})(-1 + \psi)\omega + \psi\omega^2\Big)\Big) \\ &+(2 + \psi(-2 + \omega))\Big(16\sqrt{2}(-1 + \omega) + \psi\Big(8\sqrt{2} + \omega(2 - 8\sqrt{2} + \omega)\Big)\Big)\Big),\end{aligned} \tag{B.19}$$

$$
\begin{aligned}
\hat{r}_{22} =&\frac{\zeta}{10}\left(-\gamma(-2+\omega)\left(160\sqrt{2}+\psi\left(160\sqrt{2}(-2+\psi)-10(5+8\sqrt{2})(-1+\psi)\omega+19\psi\omega^2\right)\right)\right.\\
&\left.+(2+\psi(-2+\omega))\left(160\sqrt{2}(-2+\omega)+\psi\left(160\sqrt{2}+\omega(-50-80\sqrt{2}+19\omega)\right)\right)\right),
\end{aligned}
\tag{B.20}
$$

where ζ is defined as

$$
\zeta = \frac{1}{2\sqrt{2}\psi\left(-\psi(2+\psi(-2+\omega))(-4+\omega)(-8+5\omega)+\gamma(4+\psi(-4+\omega))(-2+\omega)(8+\psi(-8+5\omega))\right)}.
\tag{B.21}
$$

Appendix C

Y/C Interface Model

The detail of this model is provided in Ref [26], which accounts for resolving of the Knudsen layer and its effects on the mass transfer scenario.

Mach number related variable for the vapor velocity is characterized as

$$S_\infty = \frac{v_v}{\sqrt{2RT_v}} = \sqrt{\frac{k}{2}}\mathrm{Ma}. \tag{C.1}$$

Temperature and pressure deviations are related to C.1 through

$$1 + \Delta\hat{T} = \frac{T_v}{T_l} = \left(\sqrt{\frac{\pi S_\infty^2}{64}} + 1 - \frac{\sqrt{\pi}S_\infty}{8}\right)^2, \tag{C.2}$$

$$1 + \Delta\hat{p} = \frac{p_v}{p_{\mathrm{sat}}\left(T_l\right)} = \frac{F + \sqrt{\frac{T_v}{T_l}}G}{2\exp\left[-S_\infty^2\right]}. \tag{C.3}$$

Here, F and G are defined as

$$F = -\sqrt{\pi}S_\infty\left(1 - \mathrm{erf}S_\infty\right) + e^{-S_\infty^2}, \tag{C.4}$$

$$G = \left(2S_\infty^2 + 1\right)\left(1 - \mathrm{erf}S_\infty\right) - \frac{2}{\sqrt{\pi}}S_\infty e^{-S_\infty^2}. \tag{C.5}$$

Reshaping C.1, using $J = \rho v$ and ideal gas law, yields the dimensionless mass flux

$$\hat{J} = 2\sqrt{\pi}\frac{1 + \Delta\hat{p}}{\sqrt{1 + \Delta\hat{T}}} S_\infty. \tag{C.6}$$

Using the equations above, by prescribing a Mach number, temperature and pressure jumps as well as the mass flux are determined. Also, substituting the determined jumps in the force equations

$$\hat{F}_J = -\frac{5}{2}\left[\Delta\hat{T} - \ln\left(1 + \Delta\hat{T}\right)\right] - \ln\left(1 + \Delta\hat{p}\right), \tag{C.7}$$

and

$$\hat{F}_Q = -\frac{\Delta\hat{T}}{1 + \Delta\hat{T}}, \tag{C.8}$$

resistivities

$$\hat{r}_{11} = \frac{\hat{F}_J}{\hat{J}}, \tag{C.9}$$

and

$$\hat{r}_{21} = \frac{\hat{F}_Q}{\hat{J}}, \tag{C.10}$$

are determined.

In Fig 4.2, we use a range of $\mathrm{Ma} \in [-0.117,\ 0.2]$ (the negative values account for condensation) to determine corresponding mass flux in the symmetric range of $\hat{J} \in [-0.465,\ 0.465]$ and resistivities within this flux range. As shown in Table 5.1, the selection $m = 3$ for the eHKS model ensures that this flux range is appropriately covered.

Appendix D

Optimization Error

To validate the data computed using the method described in Section III, we expand (2.13) as

$$\hat{F_J} = \tilde{r}_{11}\hat{J} + \tilde{r}_{12}\hat{q_v}, \tag{D.1}$$

$$\hat{F_Q} = \tilde{r}_{21}\hat{J} + \tilde{r}_{22}\hat{q_v}. \tag{D.2}$$

where we consider the values of $\tilde{r}_{\alpha\beta}$ found from the optimization method.

The relative errors are defined as

$$e_J = 1 - \frac{\tilde{r}_{11}\hat{J} + \tilde{r}_{12}\hat{q_v}}{\hat{F_J}}, \tag{D.3}$$

$$e_Q = 1 - \frac{\tilde{r}_{21}\hat{J} + \tilde{r}_{22}\hat{q_v}}{\hat{F_Q}}. \tag{D.4}$$

which are then combined into a mean-square residual error (MS)

$$e_{MS} = \sqrt{e_J^2 + e_Q^2}. \tag{D.5}$$

The MS is computed for every grid point where resistivities are calculated for both approaches of Unguided and Enforced-Symmetry, and as shown in Fig. D.1 and D.2. Both approaches demonstrate high accuracy with a maximum e_{MS} of less than 0.0004%.

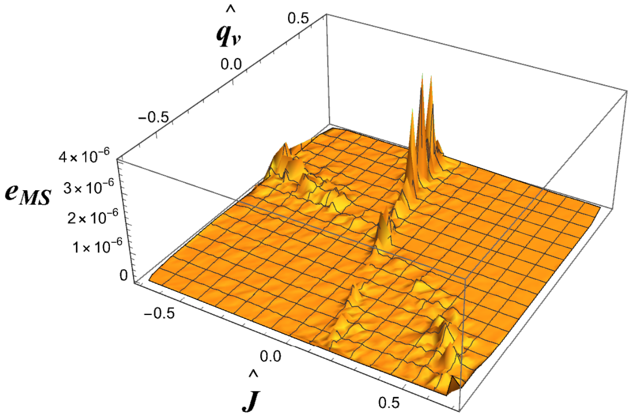

Figure D.1: The mean square residual error e_{MS} in the domain of fluxes, using Unguided approach.

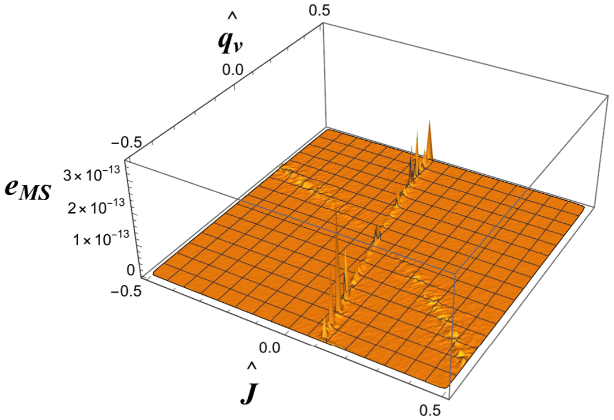

Figure D.2: The mean square residual error e_{MS} in the domain of fluxes, using Enforced-Symmetry approach.

Bibliography

[1] G. Fang and C. A. Ward. Temperature measured close to the interface of an evaporating liquid. *Phys. Rev. E*, 59(1):417, 1999. doi: 10.1103/PhysRevE.59.417.

[2] S. Homes and J. Vrabec. Resistivities across the vapor–liquid interface of a simple fluid: An assessment of methods. *Phys. Fluids*, 36(2), 2024. doi: 10.1063/5.0193522.

[3] C. A. Ward and D. Stanga. Interfacial conditions during evaporation or condensation of water. *Phys. Rev. E*, 64(5):051509, 2001. doi: 10.1103/PhysRevE.64.051509.

[4] A. Persad and C. A. Ward. Expressions for the Evaporation and Condensation Coefficients in the Hertz-Knudsen Relation. *Chem. Rev.*, 116(14):7727–7767, 2016. doi: 10.1021/acs.chemrev.5b00511.

[5] V. K. Badam, V. Kumar, F. Durst, and K. Danov. Experimental and theoretical investigations on interfacial temperature jumps during evaporation. *Exp. Therm. Fluid Sci.*, 32(1):276–292, 2007. doi: 10.1016/j.expthermflusci.2007.04.006.

[6] P. Jafari, A. Amritkar, and H. Ghasemi. Temperature discontinuity at an evaporating water interface. *J. Phys. Chem. C*, 124(2):1554–1559, 2019. doi: 10.1021/acs.jpcc.9b10838.

[7] M. Kazemi and C. A. Ward. Assessment of the statistical rate theory expres-

sion for evaporation mass flux. *Int. J. Heat Mass Transf.*, 179:121709, 2021. doi: 10.1016/j.ijheatmasstransfer.2021.121709.

[8] M. Rauter, A. Aasen, S. Kjelstrup, and Ø. Wilhelmsen. A comparative study of experiments and theories on steady-state evaporation of water. *Chem. Thermodyn. Therm. Anal.*, 8:100091, 2022. doi: 10.1016/j.ctta.2022.100091.

[9] S. Kjelstrup and D. Bedeaux. *Non-equilibrium Thermodynamics of Heterogeneous Systems.* World Scientific, 2008.

[10] H. Struchtrup and H. C. Öttinger. Nonequilibrium liquid-vapor interfaces: Linear and nonlinear descriptions. *Phys. Rev. E*, 108(6):064801, 2023. doi: 10.1103/PhysRevE.108.064801.

[11] H. Struchtrup. *Macroscopic Transport Equations for Rarefied Gas Flows.* Springer, 2005.

[12] H. Struchtrup and A. Frezzotti. Twenty-six moment equations for the Enskog–Vlasov equation. *J. Fluid Mech.*, 940:A40, 2022. doi: 10.1017/jfm.2022.98.

[13] Y. Sone and Y. Onishi. Kinetic theory of evaporation and condensation hydrodynamic equation and slip boundary condition. *Journal of the Phys. Society of Japan*, 44(6):1981–1994, 1978. doi: 10.1143/JPSJ.44.1981.

[14] Y. Sone. *Kinetic Theory and Fluid Dynamics.* Springer, 2002.

[15] Y. Pao. Application of kinetic theory to the problem of evaporation and condensation. *Phys. Fluids*, 14(2):306–312, 1971. doi: 10.1063/1.1693429.

[16] H. Hertz. Über die Verdunstung der Flüssigkeiten, insbesondere des Quecksilbers, im luftleeren Raume. *Annalen der Physik*, 253(10):177–193, 1882.

[17] M. Knudsen. Die maximale Verdampfungsgeschwindigkeit des Quecksilbers. *Annalen der Physik*, 352(13):697–708, 1915. doi: 10.1002/andp.19153521306.

[18] J. Caputa and H. Struchtrup. Interface model for non-equilibrium evaporation. *Physica A*, 390(1):31–42, 2011. doi: 10.1016/j.physa.2010.09.019.

[19] R. Meland, A. Frezzotti, T. Ytrehus, and B. Hafskjold. Nonequilibrium molecular-dynamics simulation of net evaporation and net condensation, and evaluation of the gas-kinetic boundary condition at the interphase. *Phys. Fluids*, 16(2):223–243, 2004. doi: 10.1063/1.1630797.

[20] K. Yasuoka, M. Matsumoto, and Y. Kataoka. Evaporation and condensation at a liquid surface. i. argon. *J. Chem. Phys.*, 101(9):7904–7911, 1994. doi: 10.1063/1.468216.

[21] T. Tsuruta, H. Tanaka, and T. Masuoka. Condensation/evaporation coefficient and velocity distributions at liquid-vapor interface. *Int. J. Heat Mass Transf.*, 42(22): 4107–4116, 1999. doi: 10.1016/S0017-9310(99)00081-2.

[22] R. W. Schrage. *A Theoretical Study of Interphase Mass Transfer*. Columbia University Press, 1953.

[23] M. Bond and H. Struchtrup. Mean evaporation and condensation coefficients based on energy dependent condensation probability. *Phys. Rev. E*, 70(6):061605, 2004. doi: 10.1103/physreve.70.061605.

[24] J. Cipolla Jr, H. Lang, and S. Loyalka. Kinetic theory of condensation and evaporation. ii. *J. Chem. Physics*, 61(1):69–77, 1974. doi: 10.1063/1.1681672.

[25] H. Struchtrup. *A Thermodynamic Introduction to Transport Phenomena*. Springer, 2024.

[26] T. Ytrehus and S. Østmo. Kinetic theory approach to interphase processes. *International Journal of Multiphase Flow*, 22(1):133–155, 1996. ISSN 0301-9322. doi: 10.1016/0301-9322(95)00056-9.

[27] C. Cercignani. Strong evaporation of a polyatomic gas. In *Rarefied Gas Dynamics; International Symposium, 12th, Charlottesville, VA, July 7-11, 1980, Technical Papers, Part 1*, pages 305–320, New York, 1981. American Institute of Aeronautics and Astronautics.

[28] F. Sharipov. Onsager-Casimir reciprocity relations for open gaseous systems at arbitrary rarefraction: II. application of the theory for single gas. *Physica A*, 203 (3-4):457–485, 1994. doi: 10.1016/0378-4371(94)90010-8.

[29] S. R. De Groot and P. Mazur. *Non-equilibrium Thermodynamics*. Dover Publications, 1984.

[30] H. C. Öttinger. *Beyond Equilibrium Thermodynamics*. John Wiley & Sons, 2005.

[31] V. Roldughin and V. Zhdanov. Non-equilibrium thermodynamics and kinetic theory of gas mixtures in the presence of interfaces. *Advances in colloid and interface science*, 98(2):121–215, 2002. doi: 10.1016/S0001-8686(01)00092-6.

[32] H. Struchtrup, H. Jahandideh, A. Couteau, and A. Frezzotti. Heat transfer and evaporation processes from the Enskog-Vlasov equation and its moment equations. *Int. J. Heat Mass Transf.*, 223:125238, 2024. doi: 10.1016/j.ijheatmasstransfer.2024.125238.

[33] H. Homes, A. Frezzotti, I. Nitzke, H. Struchtrup, and J. Vrabec. Heat and Mass Transfer Across the Vapor-Liquid Interface: A Comparison of Molecular Dynamics and the Enskog-Vlasov Kinetic model. *Int. J. Heat Mass Tr.*, 242:126828, 2025. doi: 10.1016/j.ijheatmasstransfer.2025.126828.

[34] T. Ytrehus. Molecular-flow effects in evaporation and condensation at interfaces. *Multiphase Science and Technology*, 9(3), 1997. doi: 10.1615/MultScienTechn.v9.i3.10.

[35] P. Virtanen, R. Gommers, T. Oliphant, M. Haberland, T. Reddy, D. Cournapeau, E. Burovski, P. Peterson, W. Weckesser, J. Bright, et al. Scipy 1.0: fundamental algorithms for scientific computing in python. *Nature Methods*, 17(3):261–272, 2020. doi: 10.1038/s41592-019-0686-2.

[36] J. Nocedal and S. J. Wright. *Numerical Optimization, 2nd ed.* Springer, 2006.

[37] H. Struchtrup. *Thermodynamics and Energy Conversion, 2nd ed.* Springer, 2024.